

**Dynamic Instabilities Imparted by CubeSat
Deployable Solar Panels**

by

Eric David Peters

S.B., Massachusetts Institute of Technology (2011)

Submitted to the Department of Aeronautics and Astronautics
in partial fulfillment of the requirements for the degree of

Master of Science in Aeronautics and Astronautics

at the

MASSACHUSETTS INSTITUTE OF TECHNOLOGY

September 2014

© Massachusetts Institute of Technology 2014. All rights reserved.

Signature redacted

Author

Department of Aeronautics and Astronautics
August 21, 2014

Signature redacted—

Certified by

.....

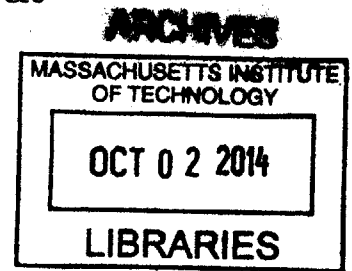
Kerri Cahoy
Boeing Assistant Professor of Aeronautics and Astronautics
Thesis Supervisor

Signature redacted

Accepted by

.....

Paulo C. Lozano
Associate Professor of Aeronautics and Astronautics
Chair, Graduate Program Committee



**Dynamic Instabilities Imparted by CubeSat Deployable
Solar Panels**

by

Eric David Peters

Submitted to the Department of Aeronautics and Astronautics
on August 21, 2014, in partial fulfillment of the
requirements for the degree of
Master of Science in Aeronautics and Astronautics

Abstract

In this work, multibody dynamics simulation was used to investigate the effects of solar panel deployment on CubeSat attitude dynamics. Nominal and partial/asymmetric deployments were simulated for four different solar panel assemblies. Trend lines were obtained for the evolution of the angular velocities and accelerations of the CubeSat about its center of mass for the duration of the deployment. The partial deployment simulations shed insight into the motions that an attitude control system may need to mitigate in the event of a deployment anomaly.

Thesis Supervisor: Kerri Cahoy

Title: Boeing Assistant Professor of Aeronautics and Astronautics

Acknowledgments

I would like to thank my advisor, Kerri Cahoy, for all of her guidance and encouragement throughout my time in graduate school.

I would also like to thank my friends and family for their support, encouragement, camaraderie, and especially for providing much-needed distractions during stressful times.

I would especially like to thank Harrison Bralower for providing me with data from tests he conducted for his own thesis. Without it, I would not have been able to validate a majority of my models.

Contents

1	Introduction	13
1.1	Motivation	13
1.1.1	Power Requirements	14
1.1.2	Dynamics Concerns	15
1.2	Organization	15
1.3	Literature Review	16
1.3.1	Dynamics of Satellites with Deployable Components	16
1.3.2	Vibration of Flexible Structures	17
1.3.3	Satellite Deployment Mechanisms	17
1.3.4	Contact Stress and Impact Modeling	19
1.3.5	CubeSat Attitude Control	20
1.3.6	CubeSat Power Systems	22
2	Methodology	23
2.1	Approach	23
2.1.1	Disturbance Metrics	24
2.1.2	Generic Configurations	24
2.1.3	Case Studies	25
2.2	Deployable Solar Panel Properties	26
2.2.1	Panel Layouts	26
2.2.2	Modeling Parameters	30
3	Analysis	35
3.1	Dynamics Model for a Single Panel	35
3.1.1	Spring Torque	37
3.1.2	Preload/Kickoff Torque	37
3.1.3	Hinge Friction	38
3.1.4	Impact Modeling	43

3.1.5	Complete Equation	47
3.1.6	Case Study 1: REXIS Radiation Cover	49
3.1.7	Case Study 2: MicroMAS Solar Panels	51
3.2	Modal Analysis of Flexible Panels	53
3.2.1	Closed-form Estimates	53
4	Software Simulations	59
4.1	Rigid Body Assumption	59
4.1.1	Chassis Model	59
4.2	Panel Vibration Modes	61
4.3	Multibody Dynamics Models	63
4.3.1	Long-edge Deployable	65
4.3.2	Double Long-edge Deployable	69
4.3.3	Short-edge Deployable	75
4.3.4	Short-edge Deployable with Long-edge Coupled	80
5	Conclusions	83
5.1	Summary of Key Results	83
5.2	Future Work	83

List of Figures

1-1	Spring-actuated hinge mechanism with end-stop and latch	18
2-1	CubeSat coordinate system	26
2-2	Long edge deployable panel configuration	27
2-3	Double long-edge deployable panel configuration	28
2-4	Double long-edge deployable panel configuration, partially stowed . .	28
2-5	Short edge deployable panel configuration	29
2-6	Short-edge deployable with long-edge coupled panel, deployed configuration	30
2-7	Short-edge deployable with long-edge coupled panel, stowed configuration	30
2-8	Composite layups used to compute bending stiffness	34
3-1	Free-body diagram of an item undergoing rotational motion	36
3-2	Hertz contact stress for two cylinders	40
3-3	Bushing friction coefficient as function of contact pressure	41
3-4	Geometry associated with a hinged punch indenting a plane	45
3-5	REXIS radiation cover test data	47
3-6	REXIS radiation cover test data with calculated angular velocity . . .	47
3-7	Comparison of dynamics model against Bralower data	50
3-8	MicroMAS solar panel dynamics model with and without friction included	52
3-9	Impact forces caused by engagement of the locking hinge	53
3-10	Sample boundary conditions and deflection curves for Rayleigh Method	54
3-11	Cross-sectional view of UTJ solar cell	55
4-1	MicroMAS bus structure finite-element model	60
4-2	First mode of MicroMAS bus structure	61
4-3	Finite-element model of single panel, short-edge constrained	62
4-4	First bending mode of single panel, short-edge constrained	62
4-5	Adams model of long-edge deployable panels	65

4-6	Comparison of deployment times between numerical and Adams deployment models	66
4-7	Dynamics of long-edge deployable with one panel stuck during deployment	67
4-8	Dynamics of long-edge deployable with one panel stuck during deployment	68
4-9	Adams model of double long-edge deployable panels	69
4-10	Predicted lower and upper bounds of deployment time for a double long-edge deployable solar panel assembly	70
4-11	Deployment angles vs. time of the exterior (top) and interior (bottom) solar panels for the double long-edge configuration.	71
4-12	Double long-edge deployable configuration with one exterior panel stuck during deployment	71
4-13	Dynamics of double long-edge deployable configuration with one exterior panel stuck during deployment	72
4-14	Double long-edge deployable configuration with one panel assembly stuck during deployment	73
4-15	Dynamics of double long-edge deployable configuration with one panel assembly stuck during deployment	73
4-16	Double long-edge deployable configuration with one panel assembly stuck during deployment	74
4-17	Dynamics of long-edge deployable with one panel assembly stuck during deployment	75
4-18	Adams model of short-edge deployable panels	75
4-19	Comparison of deployment times between numerical and Adams deployment models for a short-edge deployed solar panel.	76
4-20	Short-edge deployable configuration with one panel stuck during deployment	77
4-21	Dynamics of short-edge deployable with one panel stuck during deployment	77
4-22	Dynamics of short-edge deployable with one panel stuck during deployment	78
4-23	Short-edge deployable configuration with two panels stuck during deployment	79
4-24	Dynamics of short-edge deployable with two panels stuck during deployment	80
4-25	Adams model of short-edge deployable panels with coupled long-edge panels	80
4-26	Dynamics of short-edge deployable with two panels stuck during deployment	81

List of Tables

1.1	Reaction Wheel Models and Specifications	22
2.1	Panel Dimensions and Mass	31
2.2	Mass and inertia properties for solar panel configurations used in multi-body dynamics models	32
2.3	Spring properties used in analyses	32
3.1	Properties of hinge shaft for static Hertz contact stress analysis	40
3.2	Properties of hinge shaft for dynamic Hertz contact stress analysis	42
3.3	Comparison of properties between MicroMAS Solar Panels and REXIS Radiation Cover	46
3.4	Comparison of impact model against REXIS radiation cover test data	51
3.5	Material properties used to compute mechanical properties of panel layup	56
3.6	Results of Rayleigh Method, Short Edge Constrained, 2U Panel	56
3.7	Results of Rayleigh Method, Short Edge Constrained, 3U Panel	57
3.8	Results of Rayleigh Method, Long Edge Constrained	57
4.1	Comparison of finite-element model against prediction of Rayleigh Method, Short Edge Constrained, 2U Panel	63
4.2	Comparison of finite-element model against prediction of Rayleigh Method, Long Edge Constrained, 2U Panel	63

Chapter 1

Introduction

In this work, we investigate the dynamics associated with solar panel deployments. Our findings are useful to mission designers whose payloads or communications systems have strict pointing requirements. While the deployment dynamics of satellite solar panels have been a subject of study since the 1970s [1] [2], they have focused on large satellites whose size, mass, and power requirements are orders of magnitude larger than a typical CubeSat. We address an apparent research gap and provide detailed models and analyses of the forces and motions imparted on a CubeSat body by the deployment of solar panel assemblies.

1.1 Motivation

In recent years, the aerospace community has seen a surge in the development of inexpensive small satellites utilizing the CubeSat platform. The CubeSat standard was developed in 1999 [3] by the California Polytechnic Institute and Stanford University. The simplest platform, dubbed a “1U”, is a 10 cm cube with a maximum allowable mass of 1.33 kilograms. Satellites utilizing this form factor are popular with university programs, as they allow students to get hands-on experience developing and launching a functional space vehicle for relatively low cost compared to larger satellite missions.

Another popular CubeSat form factor is the 3U, which has dimensions 10 cm by 10 cm by 34 cm and a maximum mass of 4 kilograms. This platform has become increasingly popular with research laboratories and small companies aimed at conducting experimental science missions with rapid development timelines. Examples of these types of missions include a miniature weather satellite [4]; a space telescope for the detection of transiting exoplanets around distant stars [5]; and an optical communication demonstration [6]. These missions typically require active attitude control and larger amounts of power than their smaller 1U counterparts.

1.1.1 Power Requirements

Large spacecraft typically have solar arrays mounted to motorized actuators, which can be rotated to continuously point at the sun as the satellite travels about its orbit. In general, CubeSat solar panels are not actively controlled, and therefore may not be oriented towards the sun at all points during the orbit. In some cases it might be possible to change the orientation of the satellite to ensure optimal pointing of the solar panels, but oftentimes that is overshadowed by pointing requirements of the payload.

Additionally, the strict form factor requirements set by the CubeSat Design Specifications dictate that the CubeSat must fit within a special spring-loaded canister, called the Poly-Picosatellite Orbital Deployer (“P-POD”) for deployment on-orbit. Once the CubeSat is ejected from the deployer, there are no longer any constraints on its form factor.

The common solution, then, has been to increase the surface area of the solar panels if greater power generation is required. This has motivated the design of multi-panel, hinged solar arrays that can be compactly stowed to fit within the constraints of the P-POD for launch, but then unfold once the satellite has reached its intended orbit.

1.1.2 Dynamics Concerns

The inclusion of deployable structures on a spacecraft can introduce a number of attitude control problems that would not have existed otherwise. Likins [1] has done extensive research into modeling the response of flexible deployable structures to motions commanded by the spacecraft attitude control system. Others ([7], [8]) have studied the reaction forces and resulting motions associated with the deployment process.

Since the CubeSat is still a relatively new form factor, a large amount of the existing research into satellite dynamics is focused on large satellites. This work intends to serve as a reference to designers of CubeSat missions interested in the forces and motions imparted as a result of asymmetric solar panel deployment.

It should be noted that this thesis does not intend to study the impacts of thermal distortion caused by differential heating of the solar panels.

1.2 Organization

The remainder of this chapter dedicated to reviewing the existing body of work that was used to inform this study.

Chapter 2 develops the performance metrics against which the studied panel designs will be assessed. It also details the four solar panel configurations that will be analyzed in later sections.

In Chapter 3, a dynamics model is developed for the deployment of a single rotating panel. An overall equation of motion based on fundamental kinematic principles is used as a starting point. Equations for various external torques acting on the system are developed using parameters of the system under motion. Most importantly, a method for modeling the impact force between the rotating panel and an obstruction in its range of motion is presented. Analytical estimates of the fundamental vibration modes for various panels are also presented.

Chapter 4 discusses the simulations that were developed using commercial software packages. Finite element models of individual solar panels were created and analyzed using NEi Nastran¹. Analyses were performed for panels of length 3U constrained along the short edge and the long edge, with the first ten vibration modes being generated for each. Then, MSC SimXpert² was used to generate multi-body dynamics models of four solar panel configurations. Simulations were performed for nominal deployment as well as several partial and asymmetric deployment scenarios. Impact forces, body torques, and resulting body motions were obtained.

Chapter 5 presents the conclusions drawn from the analyses conducted in Chapters 3 and 4. A list of future work that could build on the analyses performed in this thesis is briefly discussed.

1.3 Literature Review

1.3.1 Dynamics of Satellites with Deployable Components

In the late 1960s and early 1970s, extensive research was conducted into the mathematical modeling of the resulting motions of flexible bodies attached to a rigid host body. Likins [1] published a method that introduces the concept of a “hybrid coordinate system” that uses two distinct sets of coordinate systems. The first relates to the rigid host body and is used to describe overall motions of the spacecraft, such as rotations and other motions commanded by the attitude control system. The second system relates to the normal modes of the flexible bodies and is used as a convenient way to describe the time-varying deformations of said bodies. The result is a set of equations that could be used to predict the motion induced in flexible solar panels by an attitude control maneuver of the host spacecraft.

A decade later, Christensen [9] developed a technique that utilized a nonlinear finite-element method to model dynamic response of flexible structures undergoing some

¹<http://www.nenastran.com/nei-nastran.php>

²<http://www.mssoftware.com/product/simxpert>

combination of unsteady translational and rotational motion. The primary goal of this work was to study the effect of large deformations on the motion, rather than the small deformations typically assumed by linear finite element methods.

Kuang [7] developed a simulation to investigate the resulting body motions of a satellite with . Wrote own simulation based on equations developed by Kane and Likins. Assumed reaction wheels are disabled during deployment. 100 kg satellite, 3 kg solar panels.

1.3.2 Vibration of Flexible Structures

In a 1969 technical report sponsored by the National Aeronautics and Space Administration, Leissa [10] provides a thorough compilation of the analytical methods relating to the vibration of plates. Of particular interest to this thesis are the methods related to the analysis of rectangular plates subjected to various boundary conditions. Equations are provided for the first vibration mode (and typically several more) for every possible combination of edge boundary conditions, along with the associated mode shapes.

Steinberg [11] produced a book dedicated exclusively to the analysis of electronics equipment – printed circuit boards, enclosures, etc – subjected to vibration environments. While the text from Leissa mentioned above provides a larger number of analytical methods, Steinberg serves as a reliable reference for the mechanical properties of the fiberglass epoxy laminate that is used as a substrate in printed circuit boards.

1.3.3 Satellite Deployment Mechanisms

On smaller satellites, especially CubeSats, simple mechanical elements such as torsion springs are used for actuation. Unlike with motorized hinges, the deployment rate and angle of spring-loaded hinges cannot be actively controlled. Mechanical stops must be designed into the hinge to restrict deployment from continuing beyond a

specific angle. Furthermore, to prevent the mechanism from rebounding against the mechanical stop and returning to a stowed position, a mechanical locking feature is also typically integrated into the hinge design. Impacts with the mechanical stop and the locking features result in large impulsive forces that can induce vibrations in the solar panels and possibly cause rotation of the host spacecraft.

All of the aforementioned concepts are clearly illustrated in the solar array deployment mechanism depicted in Figure 1-1. This is a commercial product developed by Surrey Satellite Technology, Ltd. to passively deploy solar arrays on their smaller, 100 kg class satellites.

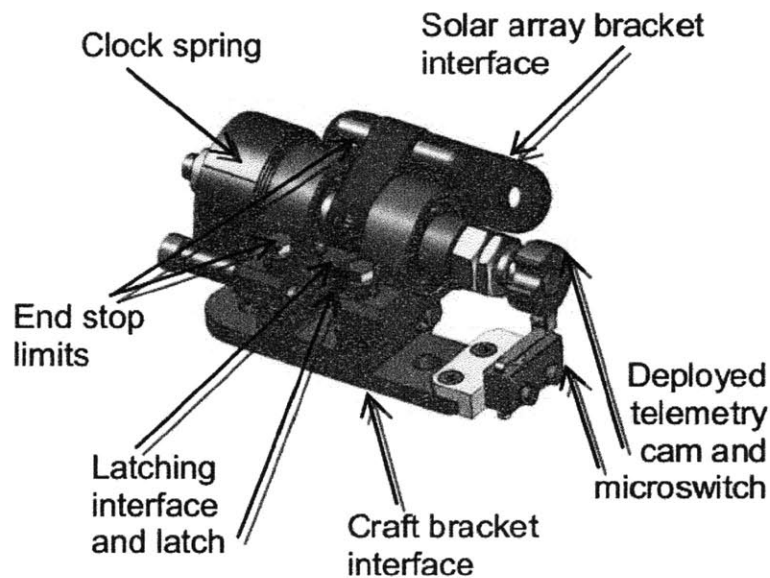


Figure 1-1: Spring-actuated hinge mechanism with end-stop and latch, from [12]

1.3.3.1 Analysis of Locking Hinges

Researchers at Shanghai Jiaotong University [8] used the professional multi-body dynamics software package MSC Adams to model the deployment of flexible solar panels for a satellite. While the specific size and mass of the satellite bus are not mentioned, it can be inferred that it falls within the minisatellite class (100+ kilograms [16])

based on the mentioned size and mass of the solar panels. In their analysis, the researchers observed an impact force of 1500 N that lasted for 0.32 seconds during the locking process. This induced a 22.03 degree/s² angular acceleration in the spacecraft. These values shall serve as an order of magnitude reference for the forces and motions predicted by this study.

Another paper reiterated the usefulness of the Adams software for simulating deployable structures on spacecraft [14]. The focus of this technical report was to highlight three built-in functions that make it possible to model two types of passive mechanisms that are commonly found on spacecraft with deployable structures. The first is a bumper that restricts the range of motion of a joint. The second is a locking feature that engages at the end of the allowable range of motion and prevents the deployable structure from rebounding to a less deployed state. These functions proved indispensable when constructing the models in Chapter 4, as no solid geometry of the assemblies being studied was available.

1.3.4 Contact Stress and Impact Modeling

Hertz contact stress is commonly used in the field of mechanical engineering when performing lifetime and failure analysis on ball bearings [15]. However, the equations commonly presented in engineering textbooks are for very specific geometries - typically small contact areas between objects with curved surfaces, such as cylinders and spheres. Determining the stress distribution for a body of arbitrary cross-section indenting against a flat surface has been a continuing source of research for decades.

In 1965 Sneddon proposed a solution that could be adapted for an object of arbitrary profile. [16] However, one limitation of his method was that the profile had to be represented as a function, which essentially restricted the application to shapes with smooth contours (such as ellipses and cones).

In another study, Chen obtained upper and lower bounds of contact pressure for a flat punch indenting a metal surface [17]. However, this study limited the profiles to a

square punch indenting a square block and a cylindrical punch indenting a cylindrical block. A more generalized method that allowed for more flexibility in the sizes and shapes of the contact areas was desired.

Fabrikant [18] devised a simple algebraic relationship between contact pressure and indentation depth of a punch of arbitrary profile into an elastic plane. Equations were obtained for various polygons and, when possible, compared to results from four previous methods. The solution error for a rectangular punch was shown to be under 2.5% for a wide range of aspect ratios, and under 10% for all of the aspect ratios surveyed. Due to its accuracy compared to other methods presented, this method was selected for use in the analysis model to determine the contact force between the deployable solar panel and its end of motion stop.

1.3.5 CubeSat Attitude Control

Two actuators that are commonly used to control the orientation of a spacecraft are reaction wheels and torque rods. Torque rods are simply electromagnets that produce torque in a given direction by acting against the Earth's magnetic field. The amount of torque that a torque rod can generate is governed by its magnetic dipole moment and the magnetic field strength of the Earth. Assuming a typical torque rod has a magnetic dipole moment of about $0.15 \text{ A}\cdot\text{m}^2$, the amount of torque that can be produced is on the order of $7.5 \times 10^{-6} \text{ Nm}$ [19].

Reaction wheels utilize the principle of conservation of angular momentum to enact changes in the satellite attitude by changing the angular velocity of a wheel, and therefore causing a reaction torque in the opposite direction. The amount of torque a reaction wheel can generate decreases as the wheel speed reaches its maximum limit. The momentum storage capability determines how long a specific wheel can operate before saturating. Once saturation occurs, the angular momentum of the wheel must be unloaded by using the magnetic torque rods to react against the Earth's magnetic field.

Several companies produce commercial-off-the-shelf products for CubeSat attitude control. These range from individual reaction wheels and torque rods to integrated attitude determination and control systems (ADCS) that include onboard microprocessing units to process attitude control algorithms, three orthogonal reaction wheels, and possibly magnetic torque coils and instrumentation – such as infrared sensors, sun sensors, or star trackers – to aid in position sensing. Products from three companies, introduced in the following paragraphs, are summarized in Table 1.1.

MAI Maryland Aerospace, Inc. produces a variety of CubeSat attitude determination and control systems. Specifications for their newest model, the MAI-400, are presented in Table 1.1. The values listed for momentum storage and maximum torque refer to the capabilities of a single reaction wheel within the unit. Similarly, the value listed for magnetic dipole moment refers to the capability of an individual torque coil. Dimensions and mass are for the entire unit.

Blue Canyon Blue Canyon Technologies is another emerging supplier of miniature reaction wheels and integrated ADCS units for CubeSats. The “XACT” integrated ADCS unit contains three orthogonal reaction wheels, a star tracker, and three orthogonal magnetic torque rods. Dimensions, mass, and reaction wheel capabilities are presented in Table 1.1. Unfortunately, no data relating to the magnetic dipole moment of the torque rods could be found.

Sinclair Interplanetary Sinclair Interplanetary is a producer of individual reaction wheels, with a product range capable of meeting the needs of CubeSats [20] through microsattelites[21]. There are presently four models available that will fit within the cross-sectional footprint of a 3U CubeSat. Given the limited volume of a 3U CubeSat, we are most interested in using the smallest models to obtain 3-axis attitude control while maximizing the amount of remaining volume for other subsystems and payload. Specifications for the two smallest reaction wheel models are presented in Table 1.1.

Table 1.1: Reaction Wheel Models and Specifications

	MAI-400	BCT XACT	Sinclair RW-0.007-4	Sinclair RW-0.01-4
Dimensions (mm)	100 x 100 x 56	100 x 100 x 50	50 x 40 x 27	50 x 50 x 30
Unit Mass (g)	694	850	90*	120*
Momentum Storage (mNm-s)	9.35	15	7	10
Maximum Torque (mNm)	0.635	6	1	1
Magnetic Dipole Moment (Am²)	0.108	-	-	-
Reference	[22]	[23], [24]	[20]	[25]

1.3.6 CubeSat Power Systems

Two commercial suppliers of CubeSat components have a number of COTS solar panel assemblies that range in complexity and power generation capabilities. While many designs are available from both vendors, there are a few designs that are vendor specific.

Pumpkin, Inc. provided an overview of their COTS solar panel assemblies in a presentation at the 2013 Small Satellite Conference. [26] Options range from single-panel deployable assemblies that generate 21W of power to multi-panel assemblies (such as the “propeller” and “turkey tail” configurations) that can generate upwards of 50W.

Clyde Space, Inc. offers a full range of CubeSat power system components, from batteries and power distribution systems to body-mounted and deployable solar panel assemblies for 1U, 2U, and 3U CubeSats. Power generation capabilities range from 7W for a single body-mounted 3U solar panel to 29W for deployable assemblies consisting of two panels each with solar cells on both sides.

Chapter 2

Methodology

2.1 Approach

A multi-step approach is taken to model the dynamics of deployable solar panels. First, a set of performance metrics are established based on state variables of the CubeSat – quantities of interest to designers of attitude control systems. Next, an equation for the motion of a single deployable panel is derived. This can be used in a numerical simulation to estimate deployment times and impact forces based on the physical properties of the item being deployed.

A commercial software package is then used to develop deployment models of four different solar panel configurations, ranging in complexity from 2 panels connected directly to the CubeSat structure to 8 panels that are connected both to the CubeSat structure and to another panel. These models are used to estimate the resulting body accelerations and rotation rates resulting from both nominal and partial deployment of the panel assemblies.

Analytical and finite-element estimations of solar panel free-vibration modes are also calculated. When used in conjunction with the model-predicted deployment impact forces, this information can be used to determine the amplitude of vibrations excited by the deployment process. It is also possible (as a subject of future work) to integrate

the finite-element vibration models with the multibody dynamics models to study any oscillatory motions that may be imparted on the CubeSat body as a result of the vibrations induced in the solar panels.

2.1.1 Disturbance Metrics

Given the limited capabilities of CubeSat attitude control components, coupled with the trend that new missions are setting increasingly strict pointing requirements, it is important to understand the disturbances that can be imparted by the deployment of structures. Many of the solar panel configurations are symmetric, and therefore should self-cancel any motions induced during deployment. There is a risk, however, that the panels do not fully deploy. If this were to occur, mission designers should have insight into the implications this could have on the mission and whether they can be corrected.

The analyses performed in this thesis will therefore be tailored to answer the following set of questions:

- What rotation rates (if any) will nominal panel deployment induce on the CubeSat?
- If a partial deployment occurs, what will be the resulting body rotation rate(s)?
- What rotation rates can an ADCS rapidly correct without wheel saturation occurring?
- What rates can be corrected over time, through some combination of reaction wheels and magnetic torque rods? How long would this take given wheel capacity and magnetic dipole strength?

2.1.2 Generic Configurations

Four deployable solar panel configurations are to be studied in this thesis: (1) long-edge deployable; (2) double long-edge deployable; (3) short-edge deployable; and (4) short-edge deployable with long-edge auxiliary panels. Each configuration is described

in further detail in section 2.2.1.3, along with any assumptions made with regard to their properties or stowed configurations.

2.1.3 Case Studies

2.1.3.1 MicroMAS Solar Panels

The Micro-sized Microwave Atmospheric Satellite (MicroMAS) is a 3U CubeSat for remote weather sensing that was jointly developed by MIT Lincoln Laboratory and the MIT Space Systems Laboratory. It was launched aboard the Cygnus-2 cargo resupply mission to the International Space Station in July 2014¹. It has four 2U deployable solar panels, mounted to the satellite in a configuration that closely resembles the “Short-edge deployable” layout discussed in subsection 2.2.1. This mission was chosen as a case study because of its relevance to the subject matter of this thesis and the availability of design data, which was heavily leveraged to influence many of the panel and hinge parameters used in the models.

2.1.3.2 REXIS Radiation Cover

The REgolith X-ray Imaging Spectrometer (REXIS) is a payload that is also under development in the MIT Space Systems Laboratory. While it is not a CubeSat and lacks deployable solar panels, it has a deployable door mechanism (the “radiation cover”) that has properties on the same order as the solar panels being studied. Analysis of this mechanism is of particular interest because there is data available from deployment dynamics tests that were conducted during the summer of 2013. Successful correlation of the simulation developed in this thesis with the existing data will serve to validate the model.

¹http://www.nasa.gov/mission_pages/station/research/experiments/1330.html

2.2 Deployable Solar Panel Properties

2.2.1 Panel Layouts

Four distinct solar panel configurations will be analyzed, based on existing commercial options. The global coordinate system used for all configurations is taken from the CubeSat Design Specifications, and is illustrated in Figure 2-1. The $+Z$ axis runs parallel to the longest dimension of the satellite, the $+X$ axis is aligned with the access ports in the CubeSat deployer, and the $+Y$ axis is oriented to complete a right-handed coordinate system.

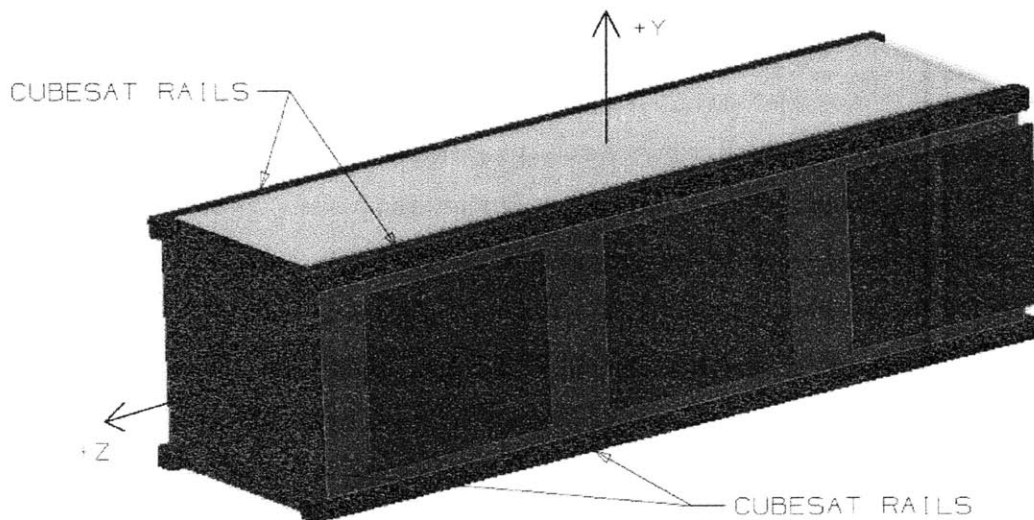


Figure 2-1: CubeSat coordinate system, from [4]

2.2.1.1 Long-edge Deployable

The first configuration contains two solar panels attached to either side of the satellite along its Z -axis. This is illustrated in Figure 2-2. When stowed, the panels are parallel with the $+X$ and $-X$ faces of the CubeSat body. At the end of deployment, both panels undergo a 90 degree rotation and end parallel to the $-Y$ face of the CubeSat body.

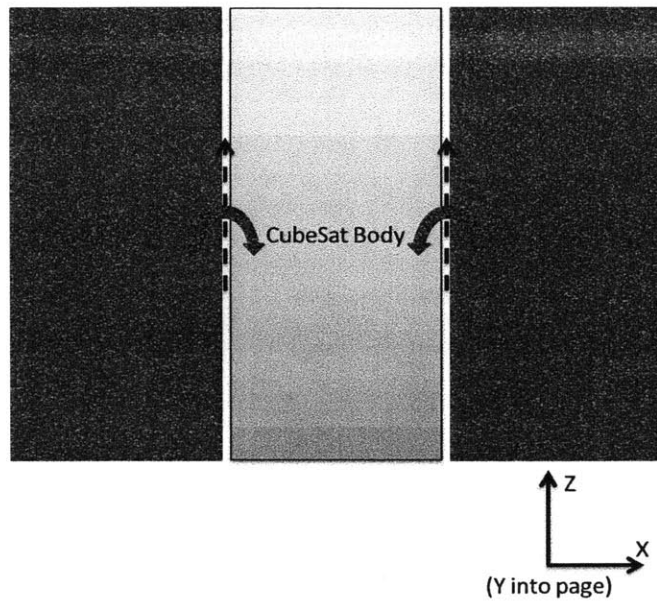


Figure 2-2: Long edge deployable panel configuration

2.2.1.2 Double Long-edge Deployable

The second configuration is an extension of the configuration shown in subsection 2.2.1.1. Again, the CubeSat body is adorned on two sides by 3U deployable panels attached along the Z -axis. However, instead of single panels being attached, there are assemblies of two panels joined along the panel long edge, as illustrated in Figure 2-3. As with the panels in the long-edge configuration, both panel assemblies are parallel to the $+X$ and $-X$ faces of the CubeSat body when stowed. Videos of deployment testing of this configuration were used to inform how the assembly folds into its stowed state. [17] [18]. The outer panels of each assembly are stowed “accordion style” and face the exterior of the assembly (as opposed to being folded to sit between the CubeSat body and the interior panel). Figure 2-4 depicts this assembly in a partially-stowed state.

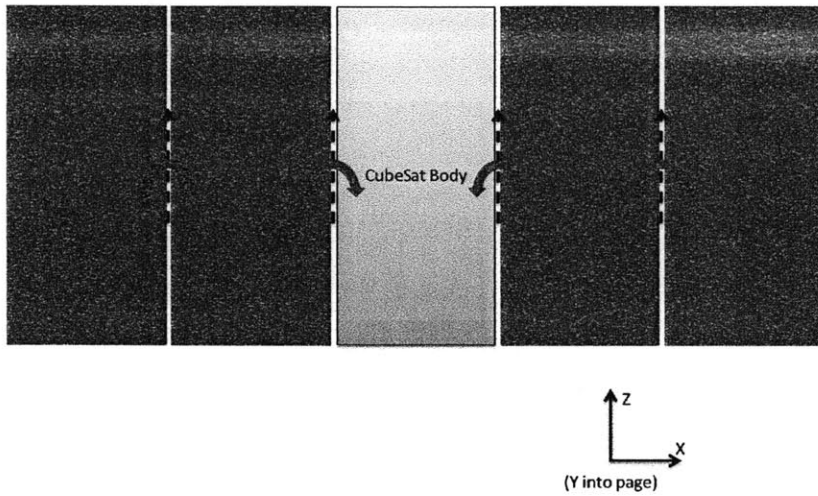


Figure 2-3: Double long-edge deployable panel configuration

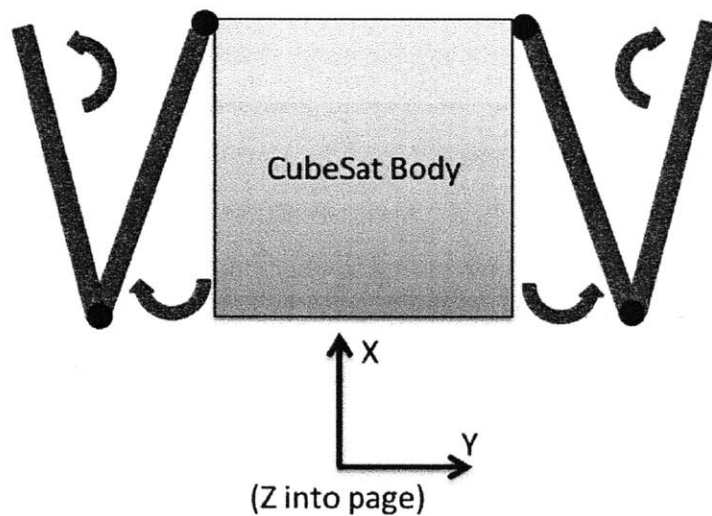


Figure 2-4: Double long-edge deployable panel configuration, partially stowed

2.2.1.3 Short-edge Deployable

The third configuration being analyzed includes four 3U solar panels attached to the base of the satellite along their short edges. Each panel is able to move independently of each other. This is illustrated in Figure 2-5.

For the general case analyzed here, the panels deploy to 90 degrees. Other deployment angles are available, however. For the MicroMAS case study, the deployment angle is

120 degrees. Another difference between the MicroMAS case study and the general case analyzed in Adams is that the MicroMAS solar panels are shorter - 2U (220 mm) instead of 3U (340 mm).

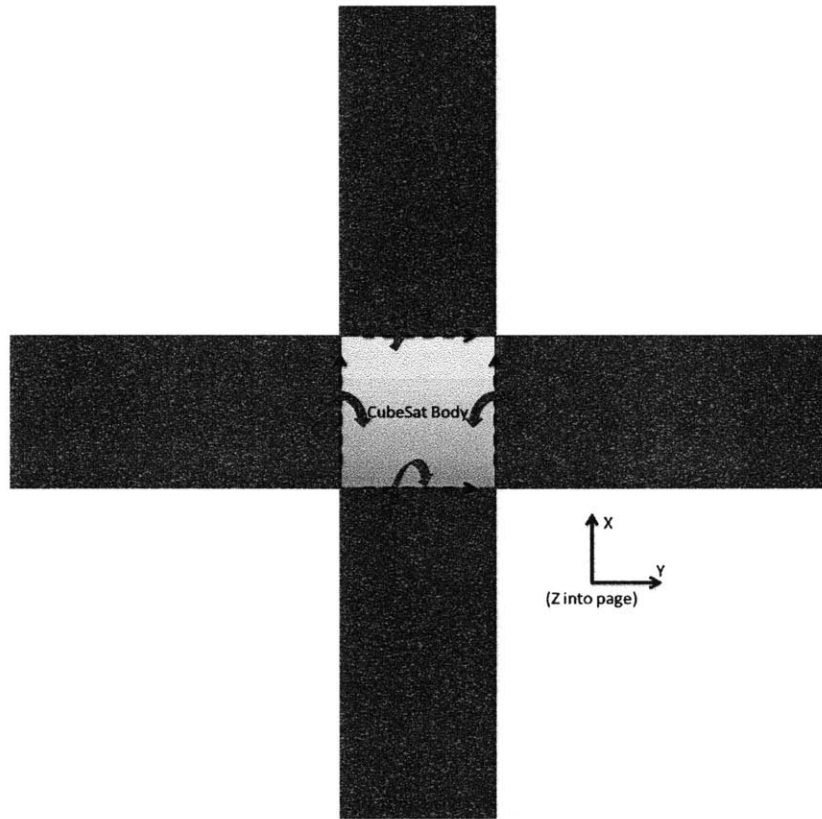


Figure 2-5: Short edge deployable panel configuration

2.2.1.4 Short-edge Deployable w/ Long-edge Coupled

The fourth configuration analyzed includes four assemblies that attach to the satellite along the short edges at the base of the bus, independent of each other. Within these assemblies, two panels are coupled together along their long edges. During model development, the panels that attach directly to the CubeSat body were dubbed the “master” panels and the auxiliary panels within each assembly were dubbed the “slave” panels. For clarity, only a single panel assembly, with its respective degrees of freedom, is illustrated in Figure 2-6. In actuality, there are four panel assemblies; one connected to each of the four free edges at the base of the satellite.

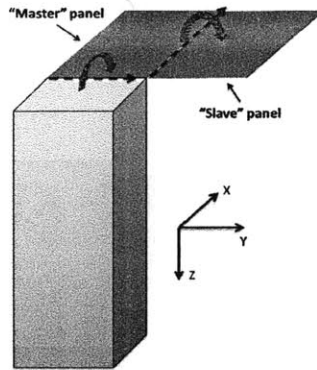


Figure 2-6: Short-edge deployable with long-edge coupled panel, deployed configuration

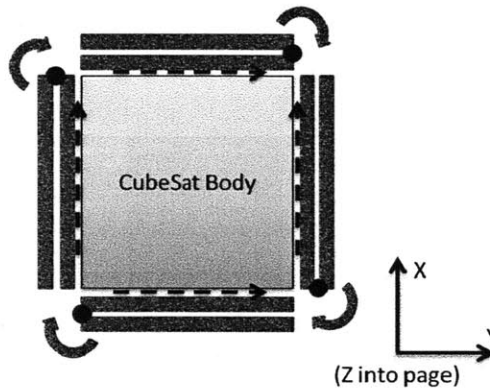


Figure 2-7: Short-edge deployable with long-edge coupled panel, stowed configuration

2.2.2 Modeling Parameters

Section 2.2.2.1 through section 2.2.2.4 describe the parameters that will be used as inputs to the analysis models, along with any assumptions made with regard to their values.

2.2.2.1 Mass

Solar Panel Mass The mass of a single 2U MicroMAS deployable panel was measured to be 0.125 kg and contained a total of 10 solar cells, 5 on each side. Using an approximate mass of 5 grams for each solar cell, the panel mass could be sepa-

rated into two contributions: 50 grams from solar cells and 75 grams for the circuit board, hinge, and other non-structural mass. Knowing the panel dimensions, it is straightforward to calculate the mass density for the panel. Extrapolating to a 7-cell double-sided 3U panel, it is fair to assume that the solar cell mass is 70 grams. Assuming the same mass density, the 3U bare panel mass is assumed to be 116g for a total 3U panel mass of 186g. The relevant properties of 2U and 3U panels are summarized in Table 2.1.

Table 2.1: Panel Dimensions and Mass

	2U	3U
Length (mm)	220	340
Width (mm)	82	82
Number of Solar Cells	10	14
Solar Cell Mass (g)	50	70
Panel Mass (g)	75	116
Total Mass (g)	125	186

Body Mass For each configuration tested, it was assumed that the total spacecraft mass is 4.0 kg. This assumption stems from the CubeSat Design Specifications [3], which states that the maximum allowable mass of a 3U CubeSat shall not exceed 4 kg. It should be noted that it is possible to apply for a waiver to exceed this mass limit (indeed, the final mass of the MicroMAS flight unit was 4.2 kg), but these waivers are assessed on a case-by-case basis and are not guaranteed to be approved. For each panel configuration, the CubeSat bus mass was adjusted appropriately to keep the entire system mass at 4.0 kg. Table 2.2 summarizes the mass and inertia properties for each panel configuration.

Table 2.2: Mass and inertia properties for solar panel configurations used in multibody dynamics models

	Long-Edge	Double Long-Edge	Short-Edge	Short- & Long-Edge
No. of Panels	2	4	4	8
Total Panel Mass (kg)	0.372	0.744	0.744	1.488
Body Mass (kg)	3.628	3.256	3.256	2.512
I_{xx} (kg m ²)	0.0426	0.0432	0.0778	0.1164
I_{yy} (kg m ²)	0.0451	0.0569	0.0778	0.1164
I_{zz} (kg m ²)	0.0104	0.0228	0.0500	0.0987

2.2.2.2 Spring Properties

One major assumption made to simplify the analysis process was that each hinge joint used the same strength torsion springs. The parameters for this spring were based on the solar panels used in the MicroMAS satellite, which is being used as a case study for the analysis model presented in Chapter 4. Relevant spring properties are presented in Table 2.3.

Table 2.3: Spring properties used in analyses

Free Angle (deg)	180
Max Torque (N m)	2.113×10^{-2}
Torque Constant (N m/deg)	1.174×10^{-4}
Number of Springs	2

2.2.2.3 Contact Area of Hinges

Another assumption made to simplify the analysis process is that all of the hinges have identical contact areas for the backstop and locking feature. Again, the parameters for these contact areas are based on the MicroMAS satellite. Contact between

the deployable solar panel and the CubeSat body occurs in two regions that have dimensions $1\text{ mm} \times 2.5\text{ mm}$. The locking feature, once it engages, has a contact region with the dimensions $1\text{ mm} \times 1\text{ mm}$.

2.2.2.4 Panel Flexibility

One of the more challenging aspects of performing the modal analysis is estimating the mechanical properties of the solar panel. At its base there is a printed circuit board that is a layup of several alternating layers of fiberglass/epoxy (FR4), copper, polyimide film (such as Kapton). Each layer of material influences the bending stiffness and other mechanical properties of the board. In addition, there are solar cells mounted on one or both sides of the panel, which also add mass and bending stiffness to the assembly. We can take a conservative approach and assume that the solar cells add mass to the assembly but do not contribute to the mechanical properties, and therefore only estimate the material properties of the bare PCB. This underestimates the bending stiffness of the panel and results in lower natural frequencies because of the additional mass from the cells. This layup is illustrated in Figure 2-8a.

The simplest way to incorporate the mechanical properties of the solar cells in the panel stiffness is to include them as external layers of the PCB layup. This method will overestimate the bending stiffness of the solar panel because it assumes that the solar cells cover the full surface area of the panel, which is not entirely accurate. Nevertheless, this is a fair assumption because for a double-sided 2U panel (dimensions 82mm by 220mm) with 5 cells per side, the solar cells cover approximately 135 cm^2 of the 178 cm^2 surface area, or 75.8%. For a double-sided 3U panel (dimensions 82mm by 340mm) with 7 solar cells per side, the solar cells cover approximately 189 cm^2 of the 275 cm^2 surface area², or 68.7%. This layup is illustrated in Figure 2-8b.

²Dimensions referenced from CAD models available from http://www.clyde-space.com/cubesat_shop/solar_panels

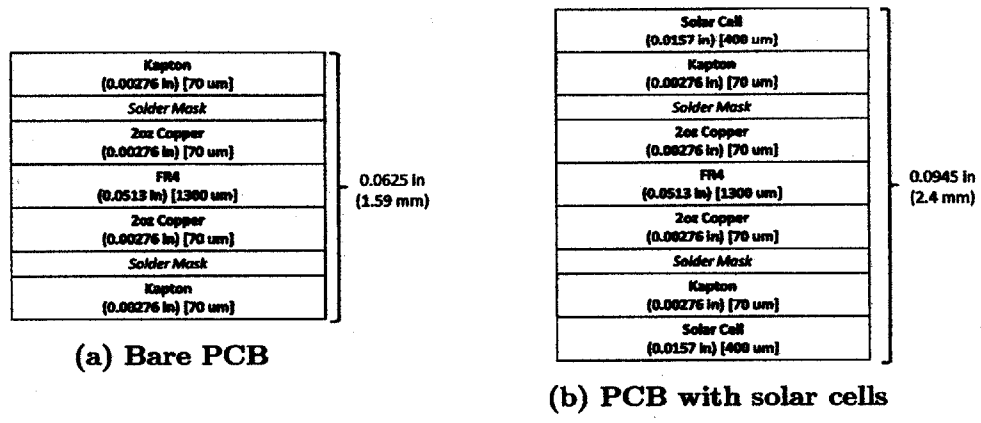


Figure 2-8: Composite layups used to compute bending stiffness

Chapter 3

Analysis

This goal of this chapter is to present the underlying physics that govern the dynamics of a single solar panel undergoing rotational motion. Terms for spring torque, static friction, dynamic friction, and kickoff spring torque are discussed. Perhaps most importantly, a method for modeling the impact force resulting from a collision between the rotating panel and an obstruction in its range of motion is discussed. A numerical simulation is programmed based on the equations developed and is used to predict the forces associated with the deployment and locking process of a single panel for the MicroMAS satellite.

3.1 Dynamics Model for a Single Panel

To develop a dynamics model for the deployment of a single panel, we must start with the basic kinematic equation for an object undergoing rotational motion, as presented in Equation 3.1.

$$\tau_{net} = I\ddot{\theta} \quad (3.1)$$

I is the moment of inertia of the solar panel, $\ddot{\theta}$ is the angular acceleration, and τ_{net} is the sum of all external torques acting on the system. To account for all factors

influencing the behavior of the system, it is important to draw a free-body diagram, shown in Figure 3-1. τ_{spring} is the torque provided by the torsion spring(s) in the hinge. It drives the motion of the panel, so its sign is positive. τ_{pre} is the preload torque caused by kickoff spring, if present in the design. This also aids the motion of the cover, so its sign is positive. $\tau_{f,dyn}$ is the torque caused by dynamic friction in the hinge. It always acts against the motion of the cover, so its sign is opposite that of the angular velocity. $\tau_{f,stat}$ is the torque caused by the static friction in the hinge, which acts only at the instant that the panel is deployed. This also acts against the motion of the cover, so its sign is negative. τ_{impact} represents the torque that is generated when the panel reaches its intended deployment angle and impacts a hard stop in the hinge. This acts against the positive motion of the panel, so its sign is negative. The full torque balance can be seen in Equation 3.2. Each term will be discussed in more detail in the following sections.

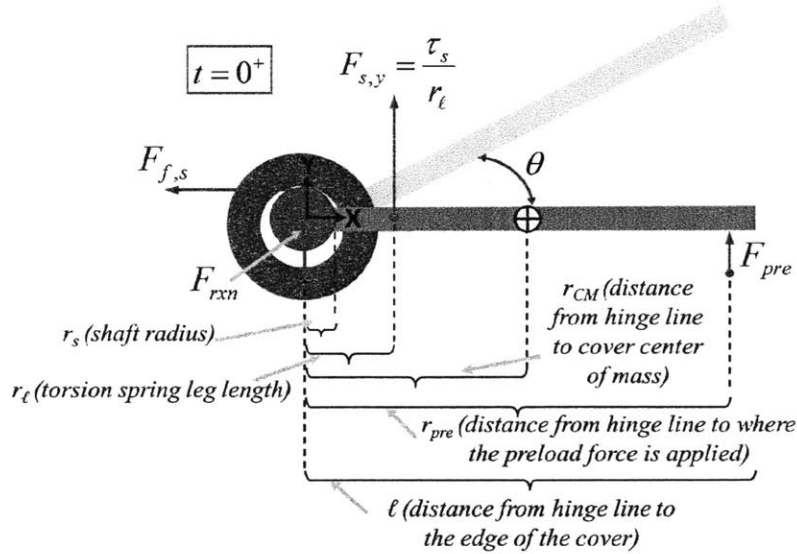


Figure 3-1: Free-body diagram of an item undergoing rotational motion from [24]

$$\tau_{net} = \sum \tau_{ext} = \tau_{spring} + \tau_{pre} - \tau_{f,dyn} - \tau_{f,stat} - \tau_{impact} \quad (3.2)$$

3.1.1 Spring Torque

Torsion springs are generally represented by an equation of the form $\tau = -k\theta$, where positive angular displacement θ is measured with respect to a zero-load angle, ϕ_0 . However, in this system, the coordinate θ is used to represent the angular displacement of the solar panel from its closed position. In this configuration, the hinge springs are oriented such that the torque provided is at a maximum when the panel is stowed and steadily decreases as the panel deploys. To account for this, the torque equation must be rewritten as shown in Equation 3.3.

$$\tau_{spring} = nk(\phi_0 - \theta) \quad (3.3)$$

Here, n is the number of torsion springs in the system, k is the torque constant of a single spring, ϕ_0 is the no-load angle of the torsion spring, and θ is the deployment angle of the solar panel.

3.1.2 Preload/Kickoff Torque

For many passive deployment systems, it is common to have the mechanism preloaded when in a closed configuration. This serves the dual purpose of preventing chatter of the mechanism due to launch vibrations and providing an additional kickoff force at the moment deployment begins. This practice is advocated in the General Environmental Verification Standard [30] (“GEVS”) developed by NASA Goddard Space Flight Center, which provides a set of standards for environmental testing of space hardware. Due to space constraints, none of the solar panel assemblies being studied in this thesis feature a mechanism that provides a kickoff force. However, the system whose test data is being used for model verification does have kickoff springs. For this reason, the kickoff torque term, shown in Equation 3.4, is being included in the general model.

The kickoff force is usually provided by a number of stiff, short-stroke linear springs

that act near the tip of the item to be deployed. This is illustrated by the F_{pre} term in the free-body diagram shown in Figure 3-1. Because of the short stroke of the springs, the force can be approximated as occurring instantaneously at the moment deployment begins. Mathematically, this is accounted for by multiplying the torque term by the Dirac delta function. F_{pre} is the “preload” force acting on the stowed mechanism by the compressed springs. r_{pre} is the distance from the axis of rotation to the point where the kickoff force is applied.

$$\tau_{pre} = r_{pre}F_{pre}\delta(t) \quad (3.4)$$

3.1.3 Hinge Friction

Models for both dynamic and static hinge friction were developed by Bralower [29] in his modeling of a deployable door mechanism for the REXIS instrument.

3.1.3.1 Static Friction

To determine the torque caused by static friction, Bralower began by recognizing that the mechanism is in static equilibrium when in the stowed position. Therefore, the static friction in the system is directly related to the normal force required to react the force provided by the torsion spring. This term is presented in Equation 3.5 [29],

$$\tau_{f,stat} = r_s\left(\mu_s\frac{\tau_s}{r_l}\right) \quad (3.5)$$

where μ_s is the static friction coefficient of the bushing material, τ_s is the total torque provided by the torsion spring(s) and r_l is the torsion spring leg length.

For the bushing material used in the MicroMAS solar panel hinges, the coefficient of friction varies as a function of the contact pressure between the hinge shaft and the bushing, as depicted in Figure 3-3. The contact pressure between the shaft and bushing is a prime example of Hertz contact stress. From Budynas [15], the

half-width, b , of the contact area between the two parts is given by Equation 3.6. The subscript 1 denotes properties related to the shaft, and the subscript 2 denotes properties related to the bushing. E and ν are the Young's modulus and Poisson's ratio, respectively, of each part; F is the contact force pushing the two parts together; l is the length of the contact region; and d is the diameter of each part. It should be noted that by convention, the diameter d is positive for convex cylinders. For a flat plane, $d = \text{inf}$. For a concave cylinder (such as a hollow tube that encompasses a shaft), d is negative. This is best illustrated in Figure 3-2.

$$b = \sqrt{\frac{2F(1-\nu_1^2)/E_1 + (1-\nu_2^2)/E_2}{\pi l \left(\frac{1}{d_1} + \frac{1}{d_2} \right)}} \quad (3.6)$$

Once the size of the contact area is known, the maximum contact pressure can be calculated as shown in Equation 3.7. In Equation 3.5, the normal force caused by the torsion springs is calculated as τ_s/r_l . Substituting the values shown in Table 3.1 into Equation 3.6 and Equation 3.7 yields a contact pressure of 7.87 MPa. The corresponding friction coefficient from Figure 3-3¹ is 0.14.

$$p_{max} = \frac{2F}{\pi bl} \quad (3.7)$$

¹http://www.igus.com/wpck/3693/iglidur_G_Werkstoffdaten?C=US&L=en

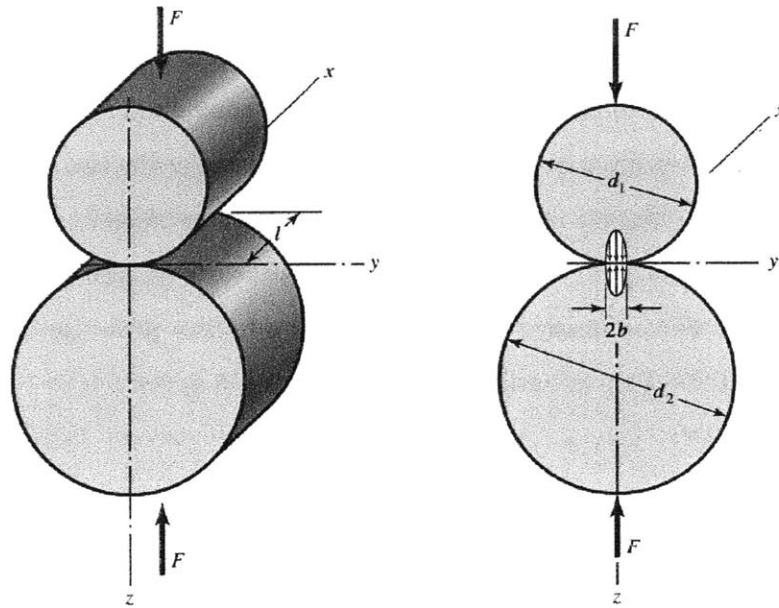
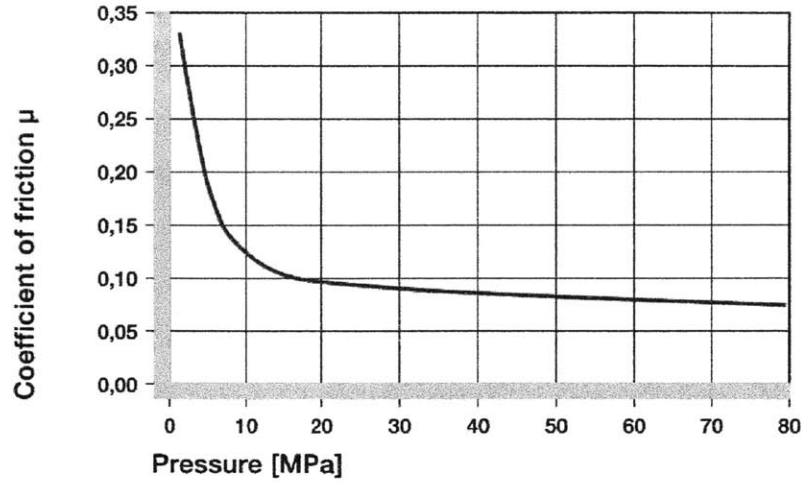


Figure 3-2: Hertz contact stress for two cylinders, from [16]

Table 3.1: Properties of hinge shaft for static Hertz contact stress analysis

d_1 (m)	1.995×10^{-3}
d_2 (m)	-2.054×10^{-3}
E_1 (Pa)	1.930×10^{11}
E_2 (Pa)	7.800×10^9
ν_1	0.27
ν_2	0.45
l (m)	6.000×10^{-3}
τ_s (Nm)	0.0423
r_l (m)	9.750×10^{-3}
μ_s	0.14



Graph 2.5: Coefficient of friction of iglidur® G as a function of the pressure

Figure 3-3: Bushing friction coefficient as function of contact pressure

3.1.3.2 Dynamic Friction

The dynamic torque in the system is dependent on the normal force at the point of contact between the hinge bushing and shaft. Bralower asserts that this force directly reacts to the centripetal force caused by the rotational motion of the cover. This term is presented in Equation 3.8 [10],

$$\tau_{f,dyn} = r_s(\mu_d m r_{CM} \dot{\theta}^2) \quad (3.8)$$

where μ_d is the dynamic friction coefficient of the bushing material, r_s is the radius of the hinge shaft, m is the mass of the panel, and r_{CM} is the distance from the axis of rotation to the center of mass of the panel. It can be seen from this equation that the dynamic friction is a function of the square of the angular velocity, making the differential equation for the dynamics model nonlinear. It is unlikely that a closed-form analytical solution exists; approximation of the solution via numerical integration must therefore be conducted.

To determine the dynamic friction coefficient, we again must find the contact pressure

between the hinge shaft and the bushing while the panel is rotating. In this situation, the normal force between the two components is a function of the angular velocity, as shown by the $mr_{CM}\dot{\theta}^2$ term in Equation 3.8. To determine this, the numerical simulation was run once without a dynamic friction torque, to produce a worst-case estimate of the angular velocity. Furthermore, since the angular velocity changes across time, the friction coefficient does as well. The friction coefficient is inversely proportional to the contact pressure, so we will take a conservative approach and use the average value of the angular velocity to determine the friction coefficient. However, the calculation is also performed using the maximum angular velocity to gain insight into the amount this coefficient changes across the range of motion of the panel. Using the maximum value for the angular velocity, the contact pressure is 3.78 MPa, resulting in a dynamic friction coefficient of 0.24. Using the average value for the angular velocity, the contact pressure is 1.69 MPa, resulting in a friction coefficient of 0.31.

Table 3.2: Properties of hinge shaft for dynamic Hertz contact stress analysis

d_1 (m)	1.995×10^{-3}
d_2 (m)	-2.054×10^{-3}
E_1 (Pa)	1.930×10^{11}
E_2 (Pa)	7.800×10^9
ν_1	0.27
ν_2	0.45
l (m)	6.000×10^{-3}
m (kg)	0.125
r_{CM} (m)	0.113
$\dot{\theta}_{max}$ (rad/s)	7.528
$\dot{\theta}_{avg}$ (rad/s)	3.764
$\mu_{d_{maxV}}$	0.25
$\mu_{d_{avgV}}$	0.31

3.1.4 Impact Modeling

The simplest method for modeling a collision between two rigid bodies is by using the theory of Hertz contact stress to determine the maximum force inside the contact region. However, this method does not account for energy dissipation during the impact [31], so a coefficient of restitution must be implemented to accordingly change the after-collision velocities of the two interacting bodies.

3.1.4.1 Contact Force

Though there does not exist an exact closed-form solution to the general form of the Hertz contact equation, extensive work has been done to develop approximate analytical solutions for a number of different contact area shapes. Equations for the impact force are adapted from Fabrikant [18], who was interested in modeling the indentation depth, w , of a flat punch under an applied load, F , into an elastic plane. This is shown in Equation 3.9.

$$w \approx \frac{HF}{g\sqrt{A}} \quad (3.9)$$

Immediately, it can be seen that this relationship follows Hooke's Law, $F = kx$, where the parameters A , g , and H act as an effective linear spring constant for the system. For our model, we are interested in determining the impact force as a function of geometry and angular displacement beyond a specified backstop angle. Therefore, Equation 3.9 must first be rearranged as shown in Equation 3.10, and then an expression approximating linear displacement from angular displacement must be determined and substituted for w .

$$F \approx \frac{gw\sqrt{A}}{H} \quad (3.10)$$

A is the area of the contact region, which has half-side lengths a and b . To account for multiple contact regions, a suitable multiplier should be included as part of the

area term. In this study, the contact regions are all of the same shape, so a multiplier n_c will be used to represent the number of contact regions. Since a and b are half-side lengths, the area of the contact region is $A = (2a)(2b) = 4ab$. The full area equation is shown in Equation 3.11.

$$A = n_c(4ab) \quad (3.11)$$

The parameter g is defined in Equation 3.12 and is specific to a rectangular region. ϵ is the ratio of side lengths, equal to $\epsilon = a/b$, where $a < b$.

$$g = \frac{2}{\pi[\sqrt{\epsilon} \sinh^{-1}(\frac{1}{\epsilon}) + \frac{1}{\sqrt{\epsilon}} \sinh^{-1}(\epsilon)]} \quad (3.12)$$

H , shown in Equation 3.13 is based on the material properties of the elastic plane that is being indented. E is the modulus of elasticity (Young's modulus) of the material, which influences how much the material deforms under an applied load. The term ν is the Poisson's ratio for the material, which represents the percentage deformation in the two axes perpendicular to the one in which a force is applied.

$$H = \frac{1 - \nu^2}{\pi E} \quad (3.13)$$

In the paper, it is assumed that the punch is perfectly rigid and the elastic plane is the only material that deforms. In reality, both the punch and the indented plane are made from elastic materials that deform under the contact force. Therefore, H needs to be modified to account for both sets of material properties. The modification is shown in Equation 3.14, where the subscripts 1 and 2 refer to the two parts that are in contact with each other. This common modification - called the "effective modulus" - can be seen in the equations presented in the mechanical design textbooks of Budynas [15] and Slocum [32].

$$H^* = \frac{1}{\pi} \left(\frac{1 - \nu_1^2}{E_1} + \frac{1 - \nu_2^2}{E_2} \right) \quad (3.14)$$

The penetration depth, w , can be approximated from the state variable θ during the numerical integration. Figure 3-4 shows an exaggerated version of the geometry associated with penetration of a rotational system.

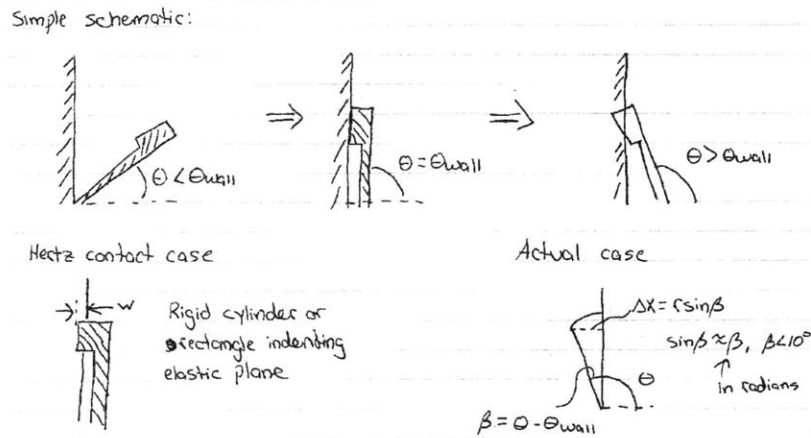


Figure 3-4: Geometry associated with a hinged punch indenting a plane

$$w \approx r_c(\theta - \theta_w) \quad (3.15)$$

θ is the deployment angle, θ_w is the angle of the rigid backstop, and r_c is the distance between the axis of rotation and the center of the contact region.

3.1.4.2 Coefficient of Restitution

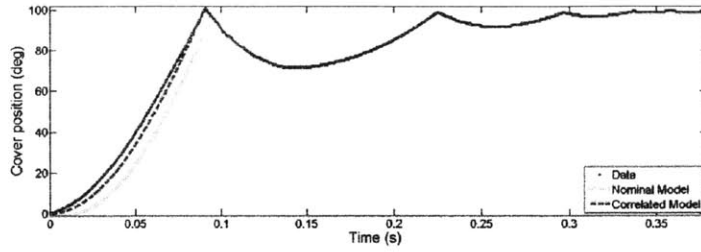
The most common method of determining restitution coefficients for various types of collisions is through experimentation. At present, there does not exist a reliable way to determine this analytically [31]. Unfortunately, it was not possible to conduct the tests required to determine this parameter for the hardware being analyzed here. However, when modeling the dynamics of the REXIS radiation cover, Bralower [29] conducted a series of tests against which he could correlate his models. Based on a

comparison between the relevant parameters of his system and the single solar panel being studied here, it appears that the two systems are sufficiently similar to allow the use of his data to determine a suitable restitution coefficient. A comparison of the relevant physical properties is provided in Table 3.3.

Table 3.3: Comparison of properties between MicroMAS Solar Panels and REXIS Radiation Cover

	MicroMAS Solar Panel	REXIS Radiation Cover
Mass (<i>g</i>)	125	54
Length (<i>mm</i>)	220	67
Width (<i>mm</i>)	82	55
<i>I</i>_{CM} (<i>kg m</i>²)	5.065×10^{-4}	2.020×10^{-5}
<i>I</i>_{hinge} (<i>kg m</i>²)	2.103×10^{-3}	3.930×10^{-5}
Number of Springs	2	2
Spring Free Angle (<i>deg</i>)	180	180
Spring Constant (<i>N m/deg</i>)	1.174×10^{-4}	1.693×10^{-4}

An example figure showing test data for deployment in a vacuum environment at room temperature with an actuation method that provides no additional deployment torque to the system is shown in Figure 3-5. The raw data obtained from Bralower did not include angular velocity, so that had to be numerically differentiated based on the discrete angular position and time data points. This is shown in Figure 3-6.



(b) Data and correlated model for the test with a solenoid at room temperature under vacuum.

Figure 3-5: REXIS radiation cover test data [30]

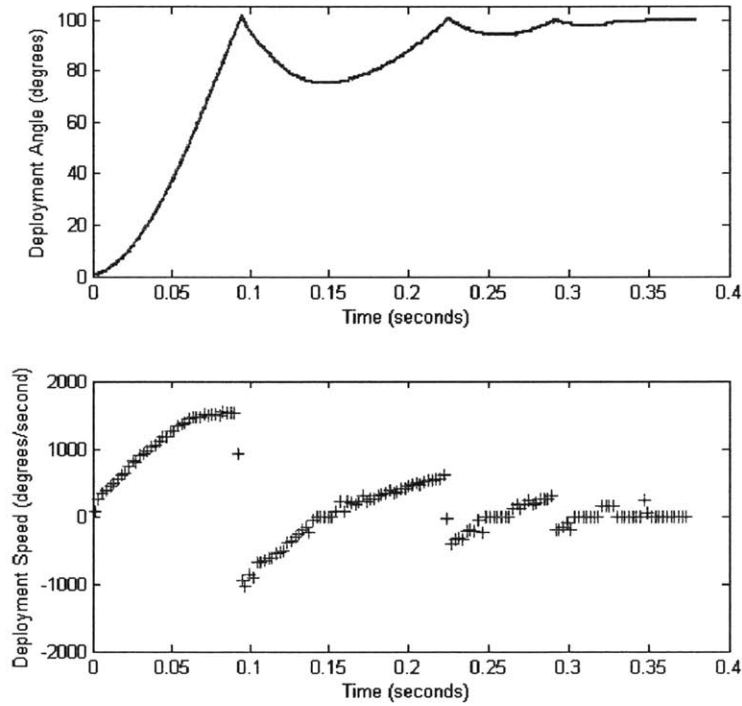


Figure 3-6: REXIS radiation cover test data with calculated angular velocity

3.1.5 Complete Equation

Combining the equations developed in Equation 3.3 through Equation 3.15 with Equation 3.2, we obtain the final equation of motion for a single panel system.

$$I\ddot{\theta} = nk(\phi_0 - \theta) - \mu_d m r_{cm} r_s (\dot{\theta}^2) - \frac{\mu_s r_s m r_s}{r_l} \delta(t) + r_{pre} F_{pre} \delta(t) + \tau_{impact} \quad (3.16)$$

The basic equation for the impact torque was derived in section 3.1.4.1. In the case where the rotating panel impacts the backstop and is free to rebound, the impact logic is simple, as seen in Equation 3.17. The logic gets more complicated if there is a locking feature that engages at the instant the panel impacts the backstop for the first time. In this situation there are two separate impact torques, governed by different sets of parameters relating to the two contact regions.

After impacting the backstop for the first time, the locking feature is engaged and prevents the panel from rebounding. The panel then immediately impacts the locking feature, which provides a force in the opposite direction. Immediately following the impact with the locking feature, the panel again impacts the backstop. This process is repeated, dissipating energy at each impact, until the panel comes to a rest.

$$\tau_{impact_{back}} = \begin{cases} 0, & 0 \leq \theta < \theta_w \\ -2\tau_c \frac{g\sqrt{n_c(4ab)}}{H^*} (\theta - \theta_w), & \theta \geq \theta_w \end{cases} \quad (3.17)$$

$$\tau_{impact_{lock}} = \begin{cases} -2\tau_c \frac{g\sqrt{n_{c,l}(4a_l b_l)}}{H_l^*} (\theta - \theta_w), & \theta < \theta_w \\ 0, & \theta \geq \theta_w \end{cases} \quad (3.18)$$

In order to solve for the dynamics of a single panel with impact forces (both with and without a locking hinge), a numerical simulation has to be developed. The simulation must perform the integration of the differential equation of motion inside of a loop. After each successful completion of the integrator, the simulation must then look at the solution vector and identify the times at which the impact began and ended. It then must use the solution state at the end of impact as the initial conditions – modified to account for the reduced velocity after the collision – for the next round

of integration. This loop continues until the panel motion is sufficiently slow.

3.1.6 Case Study 1: REXIS Radiation Cover

Before the results of this model can be trusted, they must be validated against data collected from physical testing. Due to the the expensive nature of satellite flight hardware - especially solar panels - repeated deployment testing was not possible. However, data from tests conducted by Bralower [29] in his characterization of the REXIS radiation cover was available.

Numerical estimates of the impact coefficient of restitution using the calculated velocity data shown in Figure 3-6 resulted in a range of 0.61 to 0.68, varying between data sets and also between impacts within a single test. The model was run using an average value of 0.6465, which resulted in a poor correlation between the behavior predicted by the model and the actual test data.

Through additional correlation, a suitable value for the impact coefficient was determined. For the first impact, it was found that the value was close to 0.5. Figure 3-7 shows the model output overlaid with the test data. It can be clearly seen that after the first impact, the simulated cover rebounds to the same angle that the physical cover did. However, subsequent impacts do not match the available data.

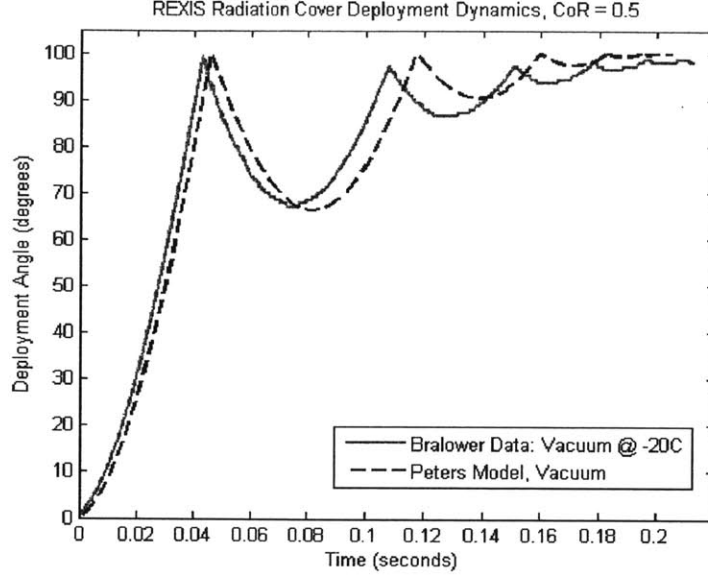


Figure 3-7: Comparison of dynamics model against Bralower data

When performing correlation between test data and his own model, Bralower [14] proposed two dynamic parameters to characterize the behavior of the system. The first was the rebound time, $t_{rebound}$, which was defined as the time it took the cover to travel from its stowed position (0°) to the angle where it first comes into contact with the backstop (102°). The second parameter was the 10%-90% rise time, t_{rise} , which was defined as the time it took to rotate between 10% and 90% of its range of motion (10.2° to 91.8°). The first parameter, $t_{rebound}$, will again be used to characterize the model. The 10%-90% rise time will not be used, however.

Instead, additional parameters must be considered in order to characterize the impact modeling algorithm, which the Bralower model did not contain. The additional parameters we will consider are the rebound angle, $\Delta\theta$, and the time between successive impacts, Δt_{impact} . The rebound angle $\Delta\theta$ is defined as the difference in angle between the rigid backstop and the local minimum to which the cover rebounds after the impact. Since the rebound angle decreases after each impact, the 10%-90% rise time was not considered a meaningful way to characterize the rebound process.

Table 3.4 summarizes the relevant performance parameters for the data set and the

model, along with the percent error between the two. The results show that for the first impact, our model does an acceptable job (i 5% error) predicting the rebound angle of the cover. However, for the second and third impacts, the model underestimates the rebound angle with increasing error. The same trend holds for the time between impacts. Between the first and second impact, the model overestimates the rebound time by 9.1%. Between the second and third impacts, however, the model begins to underestimate the rebound time.

Further investigation of the impact model should be conducted, with experimental verification if possible, to improve the fidelity of the rebound simulation. Until then, preliminary correlation against existing test data indicates that the model can simulate the first two impacts and rebound processes to an acceptable accuracy of 10%.

Table 3.4: Comparison of impact model against REXIS radiation cover test data

	REXIS Data	Peters Model	Error (%)
$t_{rebound}$, (ms)	42.8	45.7	6.8
$\Delta\theta_1$, (deg)	32.4	34.0	4.9
$\Delta\theta_2$, (deg)	10.8	9.7	-10
$\Delta\theta_3$, (deg)	3.60	2.70	-25
Δt_{impact_1} , (ms)	65.2	71.1	9.1
Δt_{impact_2} , (ms)	44.0	43.0	-2.3
Δt_{impact_3} , (ms)	28.0	23.0	-18

3.1.7 Case Study 2: MicroMAS Solar Panels

Deployment simulations were run with and without friction. As can be seen in Figure 3-8, friction does not appear to have a noticeable impact on the deployment time of the panel. For this reason it was decided that friction would be neglected in Adams models developed in the next chapter. Doing so also serves as a conservative approach to predict the worst-case accelerations one may see.

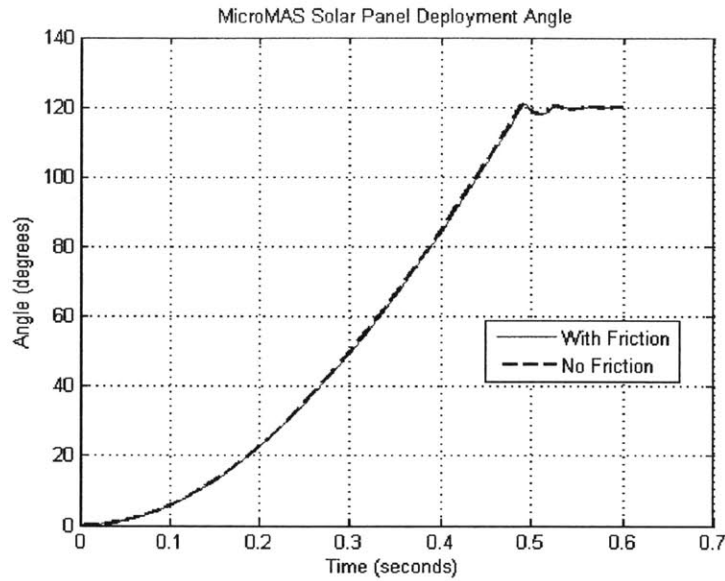


Figure 3-8: MicroMAS solar panel dynamics model with and without friction included

Figure 3-9 shows the duration and magnitude of the forces associated with the locking process. When the panel impacts the hinge for the first time, there is a large impulsive force with a peak of 3500 N acting on the panel for a duration of 0.01 seconds. The panel then rebounds and impacts the locking feature of the hinge. This was made from a more elastic material than the hinge backstop, so the impact duration is longer.

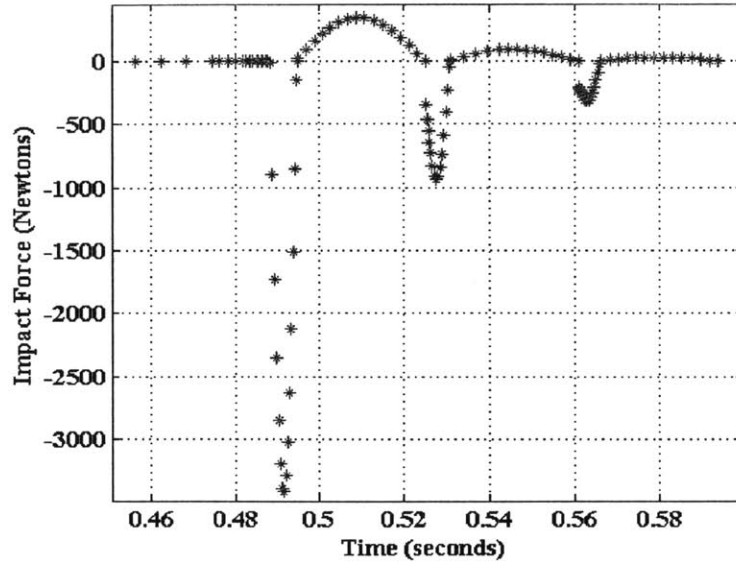


Figure 3-9: Impact forces caused by engagement of the locking hinge

3.2 Modal Analysis of Flexible Panels

One of the assumptions used when developing the model in section 3.1 was that the rotating body was rigid, eliminating the effect of vibration modes on the dynamics. This allowed us to focus primarily on the forces and torques influencing deployment and impact with the backstop and locking features (if applicable). Vibration modes are a secondary phenomenon that can be excited by these large impulsive forces, and can be studied somewhat independently of the overall body motion once estimates for the magnitude and duration of the forces are available.

3.2.1 Closed-form Estimates

In chapter 4, finite-element models of the flexible panels are developed and run to determine the first ten vibration modes. In order to validate those models, simple analytical equations can be used to estimate modes given the geometry and material properties of the panels.

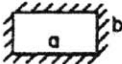
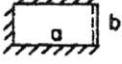
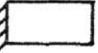
Boundary conditions	Deflection function or mode shape	N	K
	$(\cos \frac{2\pi x}{a} - 1)(\cos \frac{2\pi y}{b} - 1)$	2.25	$12 + 8 \left(\frac{a}{b}\right)^2 + 12 \left(\frac{a}{b}\right)^4$
	$(\cos \frac{3\pi x}{2a} - \cos \frac{\pi x}{2a})(\cos \frac{2\pi y}{b} - 1)$	1.50	$3.85 + 5 \left(\frac{a}{b}\right)^2 + 8 \left(\frac{a}{b}\right)^4$
	$1 - \cos \frac{\pi x}{2a}$.2268	0.0313

Figure 3-10: Sample boundary conditions and deflection curves for Rayleigh Method, from [10]

3.2.1.1 Rayleigh Method

The Rayleigh Method is one of the simpler analytical methods and is well-suited for simple geometries and boundary conditions. It approximates the board as flat plate that is constrained along some subset of its edges, and assumes the deformation can be described by a function, called a “deflection curve,” whose value meets the boundary conditions at each edge of the plate. The deflection curve for a cantilevered plate is defined as being zero at the constrained edge and maximum at the opposite edge. Sample boundary conditions and deflection curves are shown in Figure 3-10.

The first-mode frequency for a rectangular plate can be calculated using Equation 3.19 [10].

$$\omega^2 = \frac{\pi^4 DK}{a^4 \rho N} \quad (3.19)$$

In this equation, the circular frequency ω is given in radians per second, a is the side length extending from the constrained edge, ρ is the mass density per unit area of the plate, D is the flexural rigidity of the plate as defined in Equation 3.20, and N and K are parameters specific to the boundary conditions. $N = 0.2268$. $K = 0.0313$.

$$D = \frac{Eh^3}{12(1 - \nu^2)} \quad (3.20)$$

E is the Young’s modulus of the plate material, ν is the Poisson’s ratio of the material,

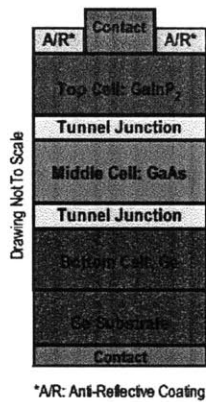


Figure 3-11: Cross-sectional view of UTJ solar cell, image courtesy of Spectrolab³

and h is the plate thickness.

3.2.1.2 Estimating Mechanical Properties

The finite-element pre-processing program Femap², produced by Siemens PLM Software, was used to calculate the bending stiffnesses and Poisson ratios for the two panel layups, illustrated in Figure 2-8a and Figure 2-8b. Femap allows you to easily model composite laminates made from multiple materials. First, a database entry was created for each of the materials used in the layup. Then a laminate was created, following the material order and thickness in Figure 2-8a and Figure 2-8b.

To model the solar cells, it was assumed that the bending stiffness primarily came from the substrate material of the cell. A cross-sectional drawing of an Ultra Triple Junction (UTJ) solar cell produced by Spectrolab, Inc., is shown in Figure 3-11. The two bottom layers of the cell are germanium, followed by a layer of gallium arsenide and a layer of gallium indium phosphate. Inspection of the solar cell datasheet shows that the bare germanium wafer thickness is $140\mu m$, which is roughly one-third of the $400\mu m$ total cell thickness.

²http://www.plm.automation.siemens.com/en_us/products/velocity/femap/

Table 3.5: Material properties used to compute mechanical properties of panel layup

Material	E (GPa)	ν	ρ (kg/m ³)	Ref
FR4	13.8	0.12	1900	[11]
Copper	110	0.343	7764	Matweb ⁷
Kapton	2.5	0.34	1420	Matweb ⁸
Germanium	130	0.30	5323	Matweb ⁹

3.2.1.3 Results

Material properties used in the analysis and results are presented in Table 3.6 and Table 3.8. Two important results are immediately noticeable. The first is that accounting for cell stiffness in the material properties of the panel layup significantly increases the first natural frequency of the panel. For both boundary conditions, the estimated natural frequency when accounting for the cell stiffness was twice as high as the estimated frequency when adding the cell mass to the stiffness of the bare PCB.

Secondly, the long-edge constrained panel is significantly more rigid than the short-edge constrained panel. Looking at Equation 3.19, it can be seen that the natural frequency is inversely proportional to the square of the cantilevered length of the panel. Since the long-edge constrained panel is roughly one third of the length of the short-edge constrained panel, it makes sense that the natural frequency is almost an order of magnitude higher.

Table 3.6: Results of Rayleigh Method, Short Edge Constrained, 2U Panel

Configuration	E (GPa)	ν	ρ (kg/m ²)	f_1 (Hz)
Bare PCB	30.6	0.29	4.148	19.5
PCB with Cell Mass	30.6	0.29	6.913	15.1
PCB with Cell Stiffness	69.1	0.298	6.913	29.1

Table 3.7: Results of Rayleigh Method, Short Edge Constrained, 3U Panel

Configuration	E (GPa)	ν	ρ (kg/m²)	f_1 (Hz)
Bare PCB	30.6	0.29	4.155	8.2
PCB with Cell Mass	30.6	0.29	6.662	6.5
PCB with Cell Stiffness	69.1	0.298	6.662	12.4

Table 3.8: Results of Rayleigh Method, Long Edge Constrained

Configuration	E (GPa)	ν	ρ (kg/m²)	f_1 (Hz)
Bare PCB	30.6	0.29	4.148	141.2
PCB with Cell Mass	30.6	0.29	6.913	109.4
PCB with Cell Stiffness	69.1	0.298	6.913	210.4

Chapter 4

Software Simulations

4.1 Rigid Body Assumption

A major assumption made in this work (and also those of Likins [1], Christiansen[9], and Kuang [7]) is that the satellite body is rigid compared to the solar panels or other appendages that are being deployed. While there may be no question about the validity of this assumption for a large satellite, one must think carefully about whether it holds true for a CubeSat. The most common structure for a CubeSat is a folded aluminum sheet metal chassis that has a wall thickness of 1.27 mm (0.050 in), which, on its own, is flexible enough to be deformed by hand if squeezed with a moderate amount of force. To assess the validity of this assumption, a simple finite-element model of the MicroMAS satellite bus was generated.

4.1.1 Chassis Model

A simple model of the MicroMAS bus structure was created using Nastran plate elements. The structure consists of the MAI-400 reaction wheel unit at the bottom, coupled to a closed rectangular tube that functions at the chassis walls. Six plates were used to model the MAI-400 unit. Coincident nodes at the corners of the plates were merged to represent the unit's solid outer shell. The MAI-400 structure was

modeled as 6061-T6 aluminum, while the chassis walls were 5052-H32 aluminum. Material properties for both metals were taken out of MMPDS-03, a metallic materials properties guide provided with the Nastran analysis program [1].

Four plates were used to model the chassis walls. The nodes along the bottom four edges of the chassis were merged with the edge nodes of the top of the MAI-400 unit to represent the joint between the two structures. In actuality, there will be bolts joining the interface plates of the two components; this joint could be better modeled in future revisions of this analysis if needed. Preliminary results indicate that this is likely not necessary. An additional plate was added to the top of the chassis walls to close the structure. Again, coincident edge nodes were merged to represent the joint between the two components.

Two sets of boundary constraints were then implemented. When the cubesat is constrained by the P-POD launcher, it is held axially (+/- Z) by the pusher plate and P-POD door, as well as in the X- and Y- directions by the P-POD rails. To implement the rail constraints, the edge nodes along the entire length of the chassis and MAI-400 were constrained in the X- and Y-translation degrees of freedom. Then, the nodes on the top and bottom faces of the chassis and MAI-400, respectively, were constrained in Z-translation to represent the P-POD door and pusher plate. This is illustrated in Figure 4-1.

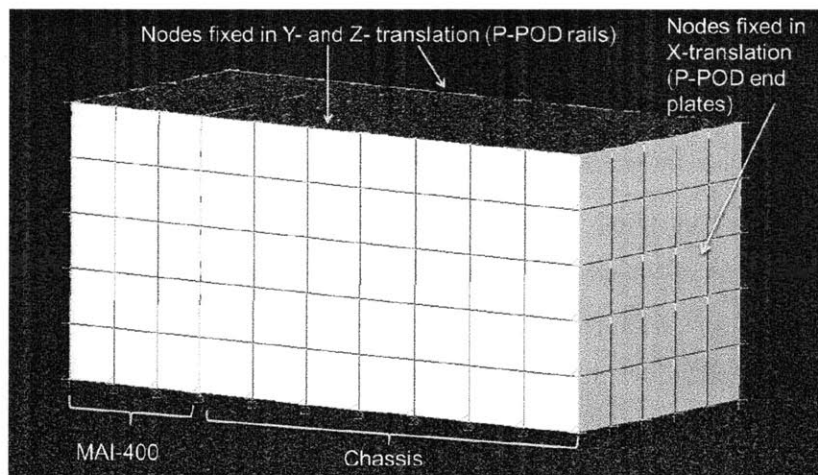


Figure 4-1: MicroMAS bus structure finite-element model

The MAI-400 internal components were represented by a point mass centered inside the unit, connected to the bottom plate. A modal analysis was then run on the structure. The first mode is a 515 Hz “breathing” mode that occurs in the chassis walls. A deformed contour plot of this mode is depicted in Figure 4-2.

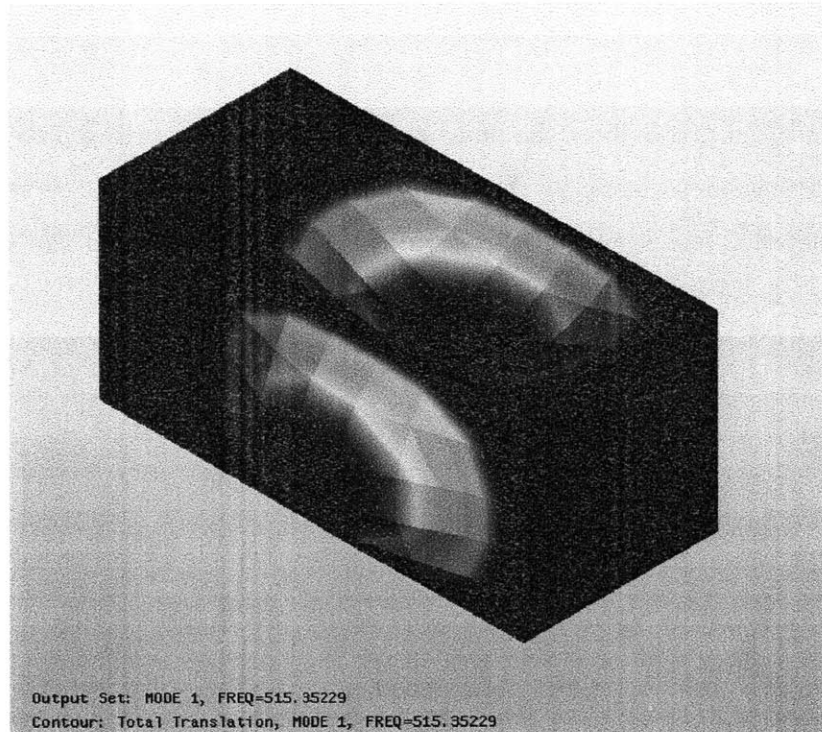


Figure 4-2: First mode of MicroMAS bus structure

The frequency of this structural mode is over 15 times greater than the first mode of a short-edge constrained deployable solar panel, and over 2 times greater than the first mode of a long-edge constrained deployable solar panel. Based on these facts, it is safe to assume that the CubeSat bus can be treated as a rigid body for the purpose of the dynamics simulations.

4.2 Panel Vibration Modes

As mentioned in section 3.2.1.2, the finite element preprocessing program Femap was used to estimate the mechanical properties of the solar panel layup. At the same

time, a simple finite element model of a 2U solar panel was constructed and solved using Nastran. Once the panel was meshed and the layup property was assigned, the mass properties of the mesh were computed. Non-structural mass was added to the layup property to make the total mass of the panel mesh match the 0.125 kg value that is being used throughout this thesis.

Figure 4-3 and Figure 4-4 show the finite element mesh and resulting first mode for the 2U panel constrained along its short edge. Table 4.1 and Table 4.2 show excellent correlation between the results of the finite element simulation and the first-mode predictions made by the Rayleigh method.

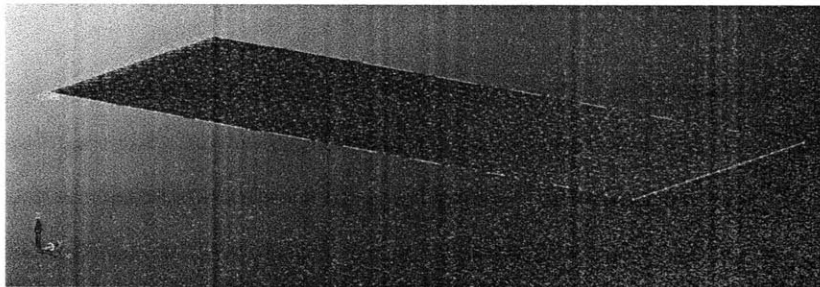


Figure 4-3: Finite-element model of single panel, short-edge constrained

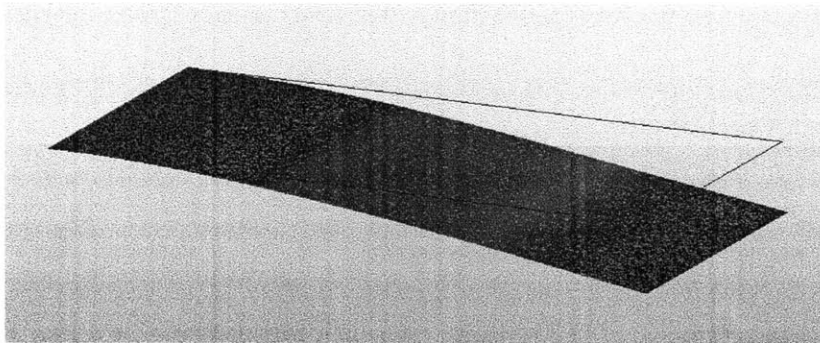


Figure 4-4: First bending mode of single panel, short-edge constrained

Table 4.1: Comparison of finite-element model against prediction of Rayleigh Method, Short Edge Constrained, 2U Panel

Configuration	f_1 - FEA (Hz)	f_1 - Rayleigh (Hz)
Bare PCB	18.3	19.5
PCB with Cell Mass	14.1	15.1
PCB with Cell Stiffness	28.5	29.1

Table 4.2: Comparison of finite-element model against prediction of Rayleigh Method, Long Edge Constrained, 2U Panel

Configuration	f_1 - FEA (Hz)	f_1 - Rayleigh (Hz)
Bare PCB	134.5	141.2
PCB with Cell Mass	104.2	109.4
PCB with Cell Stiffness	210.0	210.4

4.3 Multibody Dynamics Models

In order to analyze the deployment dynamics of the more complex multi-panel configurations, a professional software package called SimXpert was used. Developed by MSC Software Corporation, SimXpert includes the MSC Nastran solver for structural analysis – both static and modal – and the MSC Adams solver for multibody dynamics analysis.

One of the major interests of this work was to study how the motions of the CubeSat body evolve over time as solar panel deployment occurs. In orbit, the body is free to rotate about all three axes when acted on by an external torque. If the torque is constant and the satellite structure is rigid, calculating the resulting body accelerations can be straightforward. However, during solar panel deployment, several different quantities are changing with time. Among these are the moments of inertia of the satellite and the magnitude of the torque being exerted by deployment springs.

The complexity of calculating the resulting angular accelerations about the spacecraft center of mass can best be realized by studying the terms that comprise the law of

conservation of angular momentum. In its most general form, the law states that the net torque acting on a body is equal to the rate of change of its angular momentum. This is shown in Equation 4.1.

$$\vec{\tau} = \frac{d}{dt}\vec{H} = \frac{d}{dt}(I\vec{\omega}) = \frac{dI}{dt}\vec{\omega} + I\frac{d\vec{\omega}}{dt} \quad (4.1)$$

The torque, τ , and angular velocity, ω , are both vectors with components in the three body axes. The body moments of inertia, I , are a 3-by-3 matrix. Through the use of the product rule, we can gain insight into how a non-constant inertia matrix impacts the behavior of the body. Analysis of this type is best suited for numerical simulation. The commercial software package MSC Adams is a multibody dynamics physics simulator with a vast collection of algorithms and native components tailored to the simulation of dynamic systems.

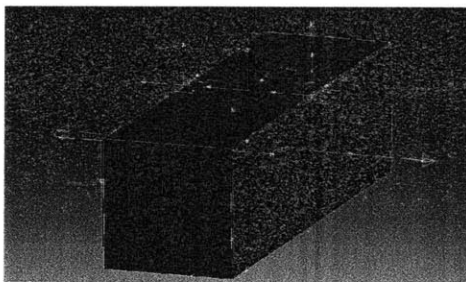
Adams has a number of native objects and functions that are ideally suited to modeling the deployment and locking of spacecraft solar panels. One set of objects is used for representing joints and connections between different parts within an assembly. The revolute joint type acts as a hinge, allowing you to restrict the motion between two parts to a single rotational degree of freedom. There are multiple ways to induce motion in the system, which include directly assigning displacements, velocities, and accelerations to parts or applying forces and torques to parts. The latter method is extremely powerful, as it allows for the modeling of self-deploying mechanisms and can even be used to restrict the joint range of motion and “lock” a part in place once deployment has occurred – all without the need for detailed 3D geometry models of such mechanisms.

The built-in linear and rotational spring objects allow you to model springs by specifying the spring constant, k and the preload force or torque exerted by the spring at a specified displacement. To restrict the range of motion of a joint, a general torque object can be created whose value is determined by a number of built-in functions. The BISTOP function allows you to specify lower and upper limits of a displacement

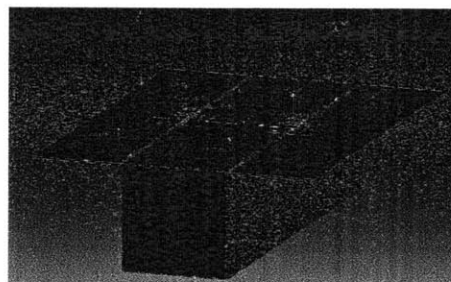
measurement (e.g. the measured angle between two bodies). If the displacement exceeds either limit, a contact force opposing the direction of motion is applied. The contact force is modeled as a stiff spring/damper system for which you can specify the spring constant and a maximum value for the damping coefficient, as well as the displacement at which full damping is applied and a modifier for the contact force.

On its own, the BISTOP function can model a situation where an object collides with a rigid stopper and is allowed to rebound freely. However, if combined with another function, it can be used to simulate a joint with a locking mechanism. As described above, a locking joint can be modeled by severely restricting the range of motion of a joint (e.g. ± 0.5 degrees above/below the desired deployment angle). However, in order to allow for normal deployment of the mechanism from its stowed position up to the desired deployment position, the BISTOP must be inactive until the deployment angle is reached. This is achieved by utilizing the unit step function, STEP, which can be configured to have a value of zero for all angles below the desired deployment angle and a value of one for all angles above. In practice, since the BISTOP function is valid for a small distance below the deployment angle, the STEP function must be shifted to allow for this. The use of these functions is covered in depth in [4].

4.3.1 Long-edge Deployable



(a) Stowed Configuration



(b) Deployed Configuration

Figure 4-5: Adams model of long-edge deployable panels

4.3.1.1 Normal Deployment

To check the validity of the Adams model, the deployment time for a single panel was compared against results predicted by the numerical simulation developed in Chapter 3. An overlay of the panel trajectories from both models can be seen in Figure 4-6. The Adams model showed a deployment time of 0.190 seconds, while the Matlab model predicted a deployment time of 0.194 seconds, for a difference of 2.1%.

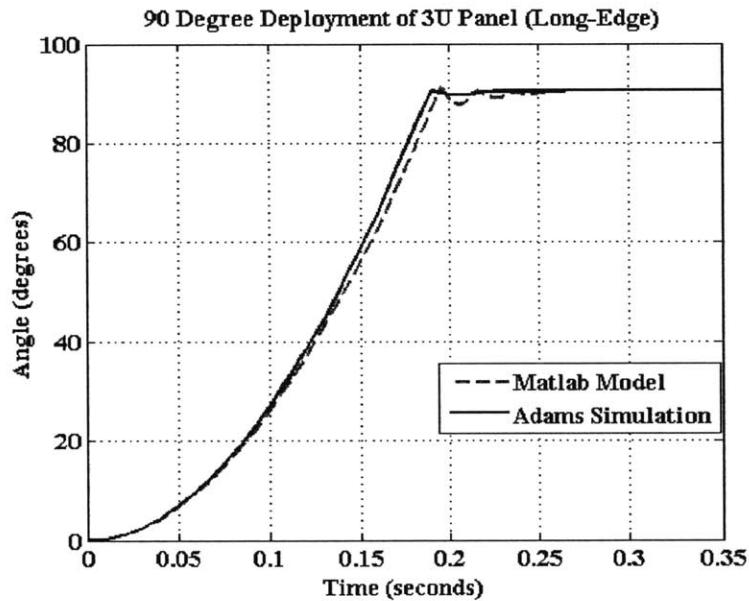
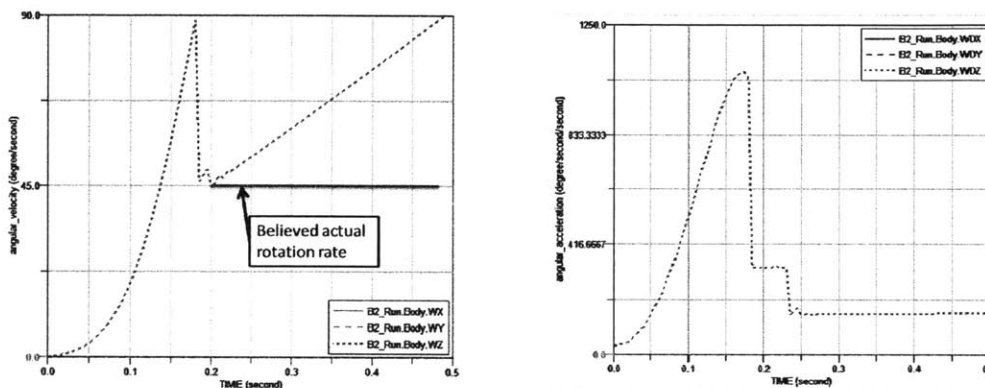


Figure 4-6: Comparison of deployment times between numerical and Adams deployment models

4.3.1.2 Off-nominal Deployment: Single Panel Stuck

The Adams simulation was then modified to study the resulting body motions in the event of an asymmetric deployment. The solar panel on the $+X$ side of the CubeSat was set to not deploy. The simulation showed no change in the deployment time for a single solar panel. At the end of deployment, the CubeSat body was left with a rotation rate of approximately 45 deg/s . Intuitively, it makes sense that an asymmetric deployment resulted in a nonzero rotation rate of the body, since the stuck panel was no longer providing an equal and opposite deployment torque.

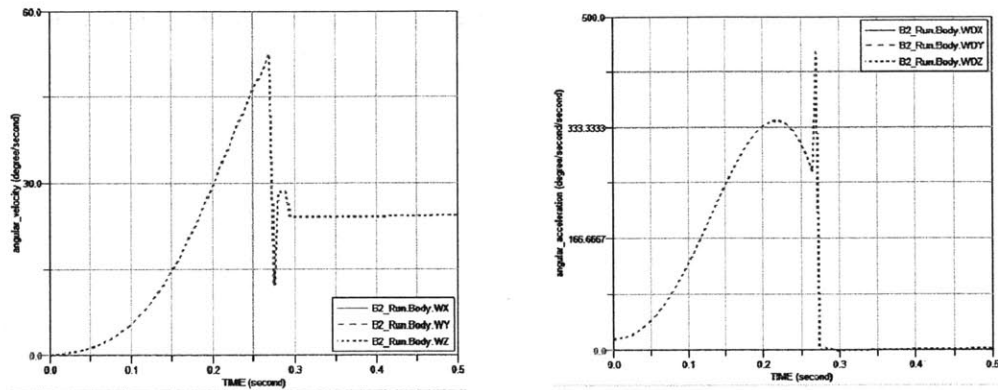
A curious trend was discovered, however, where the angular velocity continued to increase after the deployment process was complete. This can be seen in Figure 4-7a. Inspection of the angular acceleration showed that after deployment completed, the CubeSat body was left with a constant, non-zero angular acceleration about the Z-axis. This can clearly be seen for $t > 0.25$ seconds in Figure 4-7b. An investigation into the cause of this was undertaken before any further asymmetric deployments were simulated.



(a) Angular velocity about CubeSat CM (b) Angular acceleration about CubeSat CM

Figure 4-7: Dynamics of long-edge deployable with one panel stuck during deployment

The no-load angle of the torsion spring was changed from 180 degrees to 90 degrees, while the stiffness parameter k was left unchanged. This was done to observe how the simulation behaved when there was no longer a stored torque in the torsion spring when deployment was complete. The simulation results, shown in Figure 4-8, indicated that with no residual torque in the torsion spring, there was no body acceleration that continued after the solar panel completed deployment. It was worth noting that with the free-angle of the spring reduced by half, the magnitude of the torque acting on the panel when stowed was also halved. This had the expected impact of increasing deployment time from 0.19 seconds to 0.27 seconds. The weaker torsion spring also reduced the final rotation rate of the body to approximately 25 deg/s.



(a) Angular velocity about CubeSat CM (b) Angular acceleration about CubeSat CM

Figure 4-8: Dynamics of long-edge deployable with one panel stuck during deployment

An additional simulation was run to further investigate this behavior. This time, the spring constant for the torsion spring was doubled, that way the preload torque acting on the stowed panel was identical to the actual configuration. The free angle of the torsion spring was again set to 90 degrees. Results showed a reduced deployment time, back to $t = 0.19$ seconds, and an increased body rotation rate of approximately 35 deg/s.

Based on the results of these two additional simulations, the 45 deg/s rotation rate seen in Figure 4-7 at the instant deployment ends is believed to be accurate. The tendency for that to increase with time afterwards is not believed to be accurate, however. It is highly suspected that the rotation rate is actually constant, and not increasing.

4.3.2 Double Long-edge Deployable

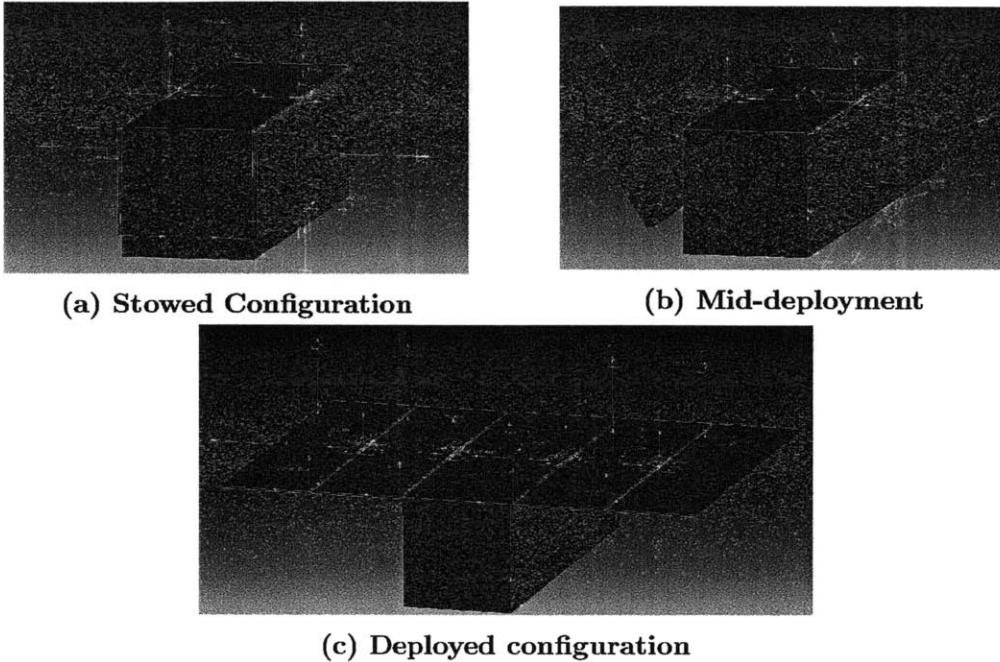


Figure 4-9: Adams model of double long-edge deployable panels

4.3.2.1 Normal deployment

Modeling the deployment of this coupled assembly is not a trivial task, since the moment of inertia of the overall assembly changes throughout the deployment process. Additionally, prediction of any coupling that may occur between motions of the exterior and interior panels is not intuitive. Two runs of the numerical simulation developed in Chapter 3 were performed to generate lower and upper bounds of deployment time for the interior solar panels. The lower bound corresponds to the inertia of the panel assembly at the moment deployment begins – the exterior panel is still stowed against the interior panel, so the assembly center of mass is closest to the axis of rotation. The upper bound corresponds to the inertia of the panel assembly at the end of deployment – the exterior panel is fully deployed, so the assembly center of mass is farthest from the axis of rotation. Both deployment trajectories are shown in Figure 4-10.

Figure 4-11 shows the deployment angles for the interior and exterior panels of a double long-edge panel assembly. The top plot corresponds to the deployment angle of the exterior panel relative to its stowed position against the interior panel. The bottom plot corresponds to the deployment angle of the interior panel relative to its stowed position against the side of the CubeSat body. An interesting trend is observed. Once the exterior panel reaches its full deployment angle, there is a significant change in the slope of the deployment angle curve for the interior panel. This can likely be attributed to the fact that the inertia of the assembly is no longer changing. The total deployment time for the assembly is 0.335 seconds, which falls within the range of times predicted by Figure 4-10.

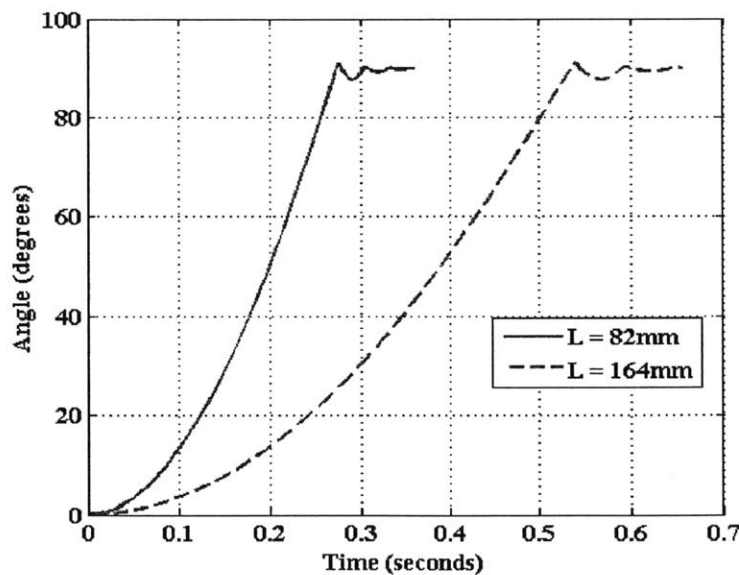


Figure 4-10: Predicted lower and upper bounds of deployment time for a double long-edge deployable solar panel assembly

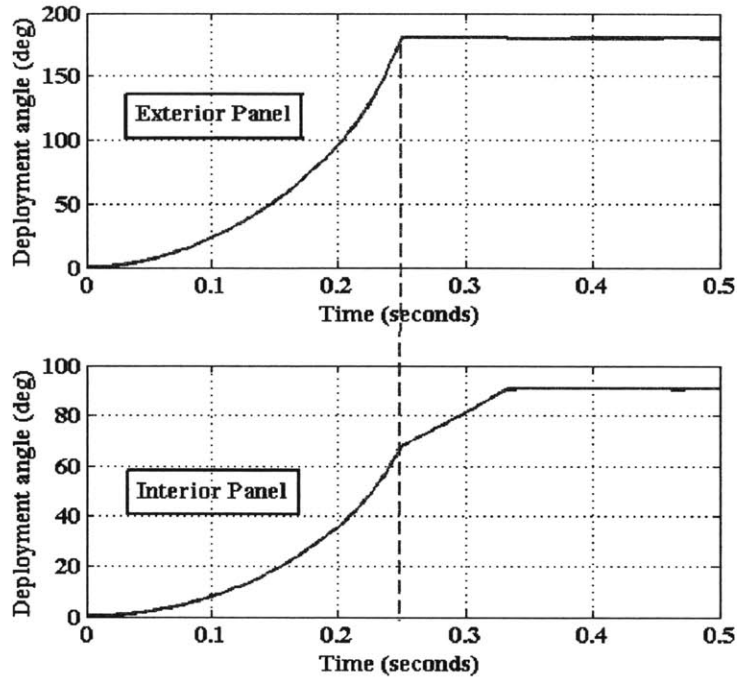
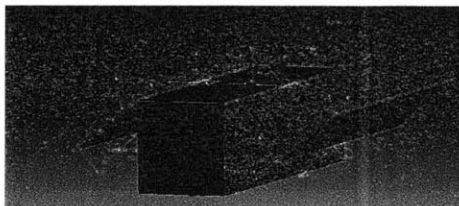


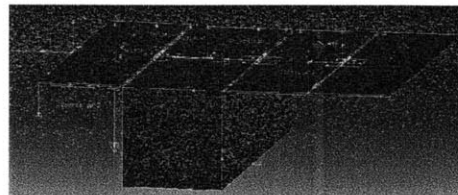
Figure 4-11: Deployment angles vs. time of the exterior (top) and interior (bottom) solar panels for the double long-edge configuration.

4.3.2.2 Off-nominal Deployment: Outer Panel Stuck

For the first off-nominal deployment case, it was assumed that one of the exterior panels failed to deploy. In Adams, motion of the exterior panel on the +X side (“Xp2”) was disabled. No changes were made to the free angle or torque constant for any of the torsion springs. Figure 4-12 illustrates this scenario during and at the end of deployment.



(a) Mid-deployment

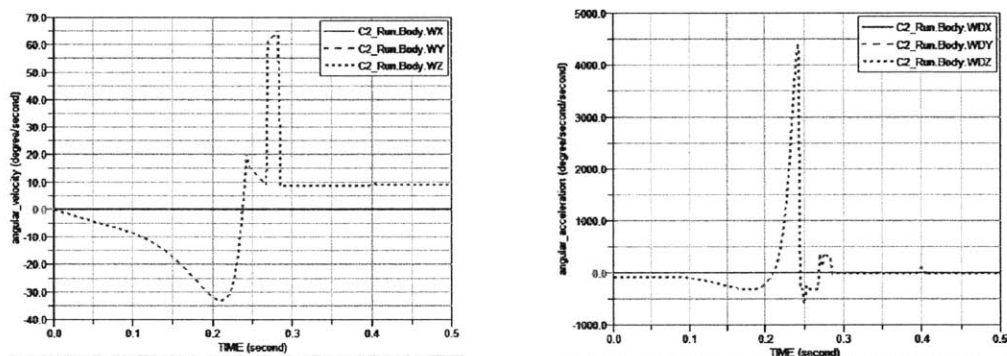


(b) Final deployed state

Figure 4-12: Double long-edge deployable configuration with one exterior panel stuck during deployment

Figure 4-13 shows the angular velocities and accelerations of the CubeSat body about its center of mass during and after deployment. After deployment, the satellite is left with an angular velocity of approximately 10 deg/s about its Z-axis, as seen in Figure 4-13a.

The spike in angular acceleration around $t = 0.25$ seconds corresponds to the exterior panel (Xn2) on the -X side reaching full extension and impacting the hinge backstop. Physically, it makes sense that the largest body acceleration is caused by the deployment impact of this exterior panel because the impact force is acting over a large lever arm. The spike in angular velocity around $t = 0.27$ seconds corresponds to the +X solar panel assembly reaching full extension and impacting the hinge backstop.

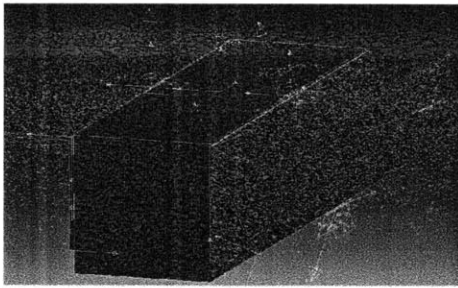


(a) Angular velocity about CubeSat CM (b) Angular acceleration about CubeSat CM

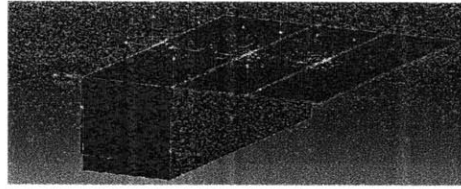
Figure 4-13: Dynamics of double long-edge deployable configuration with one exterior panel stuck during deployment

4.3.2.3 Off-nominal Deployment: Entire Side Stuck

For the next scenario, both solar panels on the +X side of the CubeSat were set to remain in their stowed positions. Figure 4-14 illustrates this scenario during and at the end of deployment.



(a) Mid-deployment

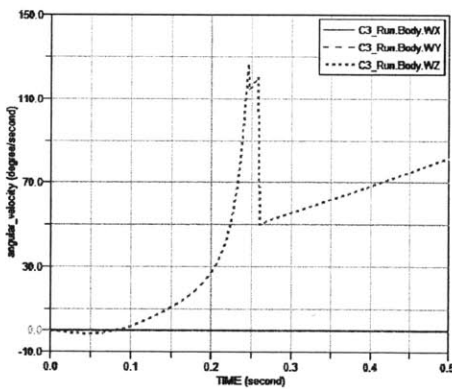


(b) Final deployed state

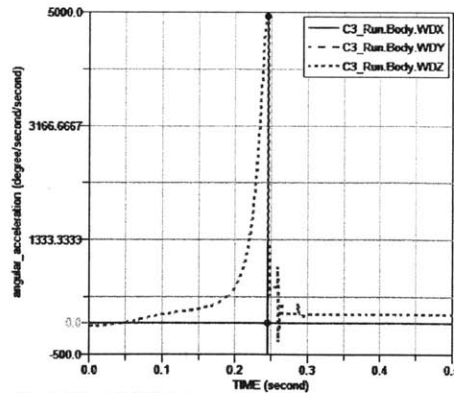
Figure 4-14: Double long-edge deployable configuration with one panel assembly stuck during deployment

At the end of deployment, the satellite is left with an angular velocity on the order of 50 deg/s about its Z-axis. It is important to note that this is believed to be a constant velocity, despite the trend line in Figure 4-15a continuing to increase with time. As with the asymmetric deployment case in 4.3.1.2, the angular acceleration is believed to be an artifact of the numerical simulation, resulting from how the preload in the torsion springs is modeled.

Again, the spike in angular acceleration around $t = 0.24$ seconds corresponds to the impact and locking of the exterior panel on the -X side of the satellite.



(a) Angular velocity about CubeSat CM



(b) Angular acceleration about CubeSat CM

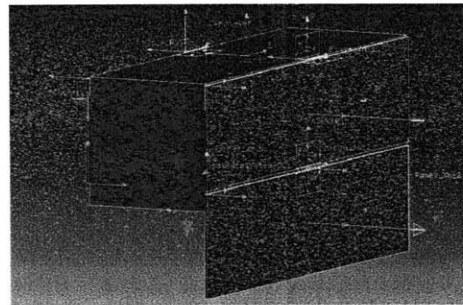
Figure 4-15: Dynamics of double long-edge deployable configuration with one panel assembly stuck during deployment

4.3.2.4 Off-nominal Deployment: One Exterior Panel Only

The final scenario studied for this panel configuration was the event that all solar panels fail to deploy, except for a single exterior panel. Figure 4-16 illustrates this scenario during and at the end of deployment.



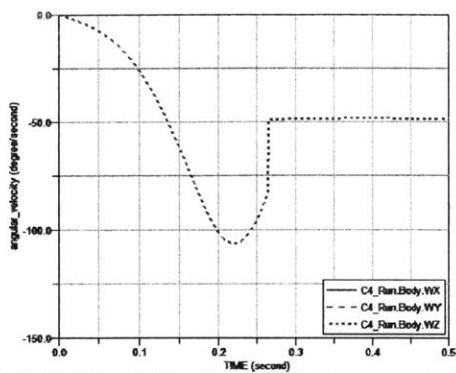
(a) Mid-deployment



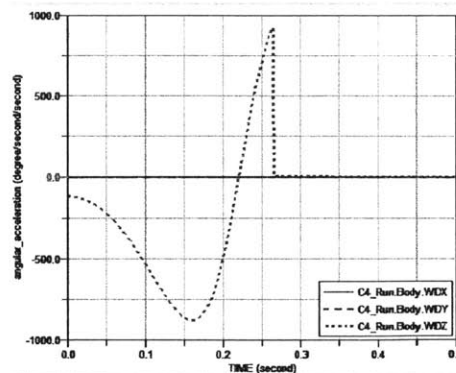
(b) Final deployed state

Figure 4-16: Double long-edge deployable configuration with one panel assembly stuck during deployment

At the end of deployment, the satellite is left with a rotation rate of **-50 deg/sec** about its Z axis. Because the deployed state of the exterior panel is 180 degrees away from its stowed position, the torsion springs release all of their stored energy during deployment and end at their no-load angle. The simulation quirk observed in the previous section resulting from stored torque in the spring is therefore not an issue for this case.



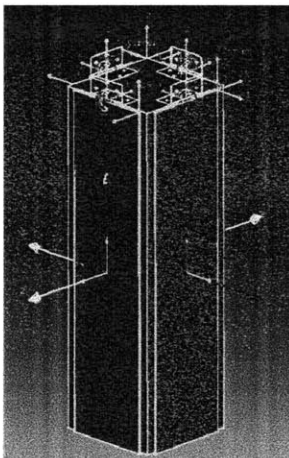
(a) Angular velocity about CubeSat CM



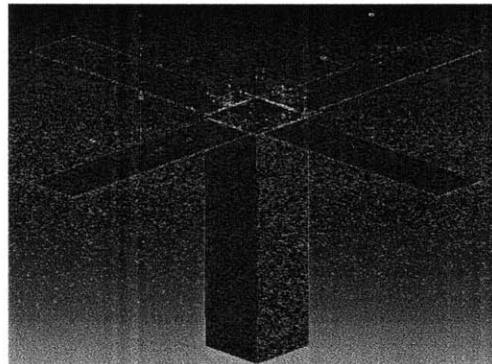
(b) Angular acceleration about CubeSat CM

Figure 4-17: Dynamics of long-edge deployable with one panel assembly stuck during deployment

4.3.3 Short-edge Deployable



(a) Stowed Configuration



(b) Deployed Configuration

Figure 4-18: Adams model of short-edge deployable panels

4.3.3.1 Nominal Deployment

Since this configuration does not contain any coupled multi-panel assemblies, the deployment dynamics for a single panel can be directly compared to the results of the numerical simulation developed in Chapter 3. The panel trajectories from both simulations are presented in Figure 4-19. The Adams model predicted a deployment

time of 0.765 seconds. The Matlab model predicted a deployment time of 0.775 seconds, for a difference of 1.3%.

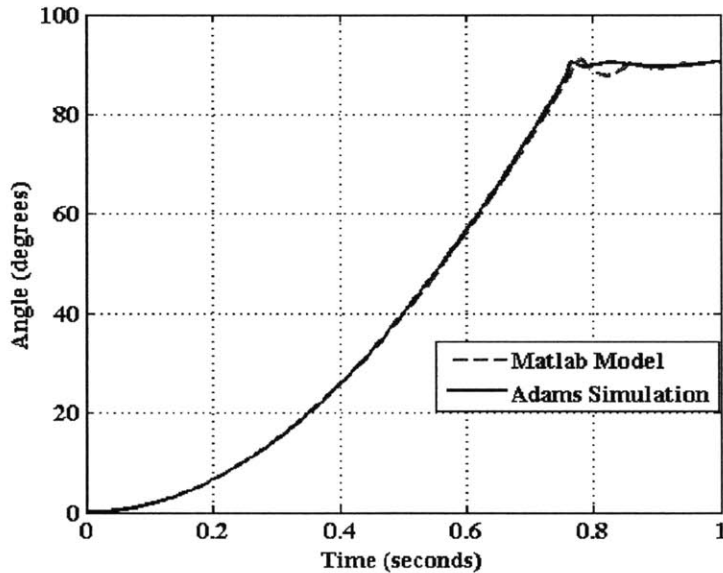
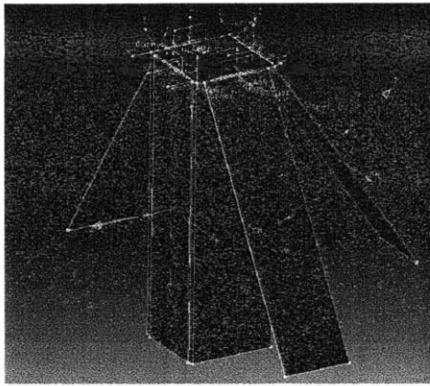


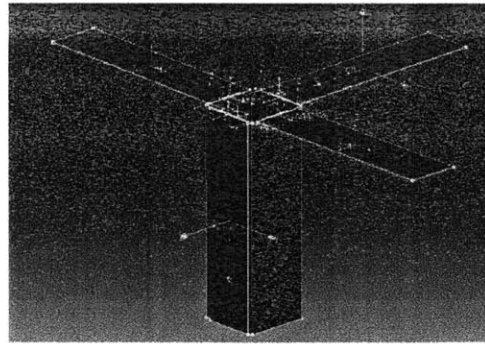
Figure 4-19: Comparison of deployment times between numerical and Adams deployment models for a short-edge deployed solar panel

4.3.3.2 Off-nominal Deployment: Single Panel Stuck

The first off-nominal deployment case studied for this configuration was a single panel not deploying. The Adams model was modified to have the +X solar panel remain in its stowed state. Figure 4-20 illustrates this scenario during and at the end of deployment.



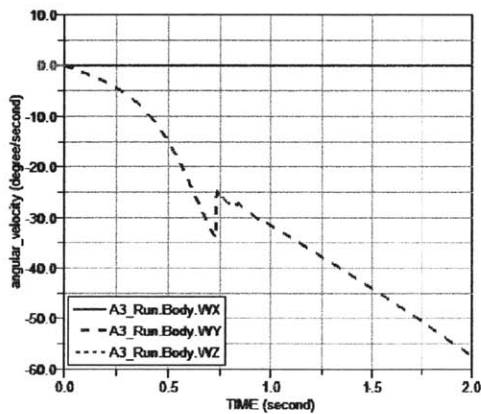
(a) Mid-deployment



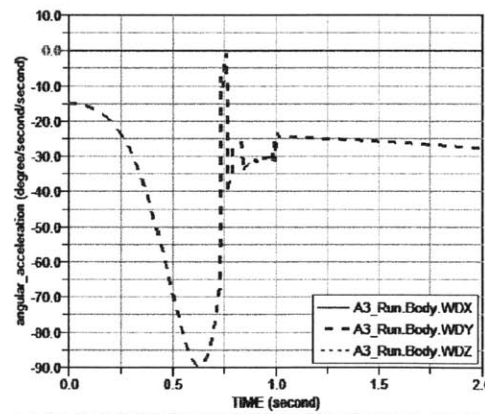
(b) Final deployed state

Figure 4-20: Short-edge deployable configuration with one panel stuck during deployment

At the end of deployment, the satellite is left with an angular velocity of -25 deg/s about its Y axis. Again, the post-deployment data shows the angular velocity steadily increasing with time, which is consistent with the fact that there is preload remaining in the torsion spring. It is suspected that the angular velocity is actually constant.



(a) Angular velocity about CubeSat CM

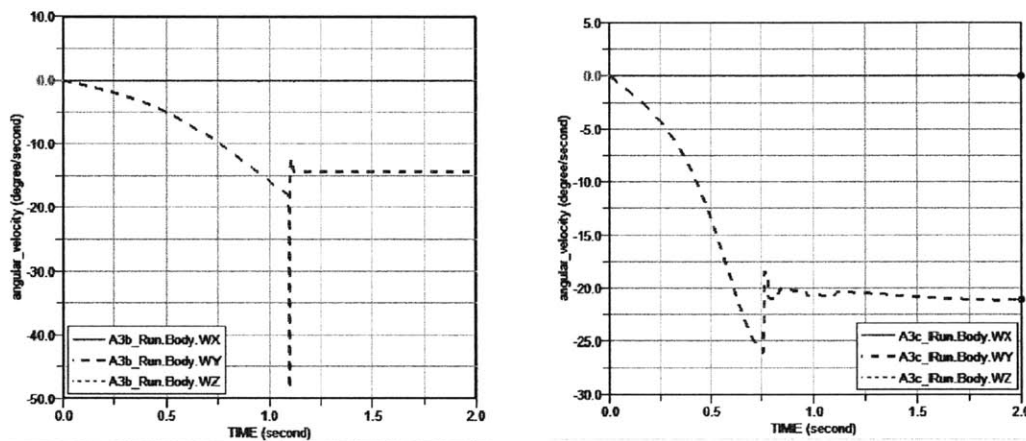


(b) Angular acceleration about CubeSat CM

Figure 4-21: Dynamics of short-edge deployable with one panel stuck during deployment

A similar procedure as was done in 4.3.1.2 was used to check the magnitude of the resulting angular velocity. Figure 4-22 shows the results for two additional simulations. In (a) the free-angle of the torsion spring was changed from 180 degrees to

90 degrees, to ensure there was no preload remaining in the torsion spring when the panel was fully deployed. The spring constant was unchanged from its nominal value of $k = 2.347 \times 10^{-4}$ N m/deg, so the maximum torque provided by the spring against the stowed panel was 2.113×10^{-2} N m – half of its nominal value. In (b) the free-angle of the torsion spring was again changed from 180 degrees to 90 degrees. Additionally, the spring constant was doubled, to $k = 4.695 \times 10^{-4}$ N m/deg. This had the effect of providing the nominal torque of 4.226×10^{-2} N m against the stowed panel.



(a) Angular velocity about CubeSat CM (b) Angular acceleration about CubeSat CM

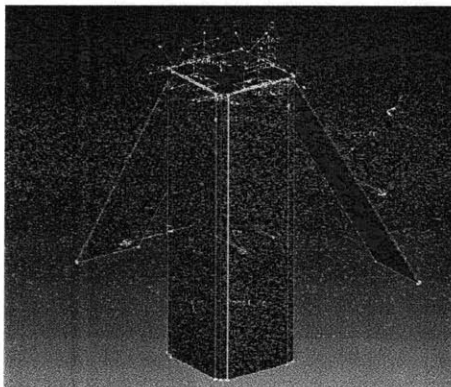
Figure 4-22: Dynamics of short-edge deployable with one panel stuck during deployment

Both simulations resulted in the satellite body having a constant angular velocity about the Y axis at the end of the deployment process. With the weaker torsion spring, the simulation shown in Figure 4-22a had a final rotation rate of **-14 deg/s**. The stiffer torsion spring used in Figure 4-22b shows a post-deployment angular velocity of **-20 deg/s**.

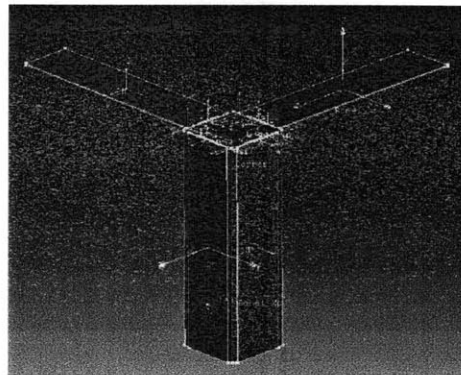
Based on the magnitudes of the post-deployment angular velocities from these two additional simulations, we believe it is fair to conclude that the post-deployment velocity in Figure 4-21a is a constant **-25 deg/s**.

4.3.3.3 Off-nominal Deployment: Two Panels Stuck

The next deployment scenario simulated two orthogonal panels failing to deploy. In addition to the +X panel that was fixed in the previous scenario, the +Y panel was commanded to remain in its stowed position throughout the simulation. Figure 4-23 illustrates this scenario during and at the end of deployment. As expected, due to the symmetry of the panels, the angular velocity and angular acceleration curves about the X and Y axes are identical. It can then be concluded that with two orthogonal panels stuck during deployment, the CubeSat will have angular velocity components about the X and Y axes of **25 deg/s**.

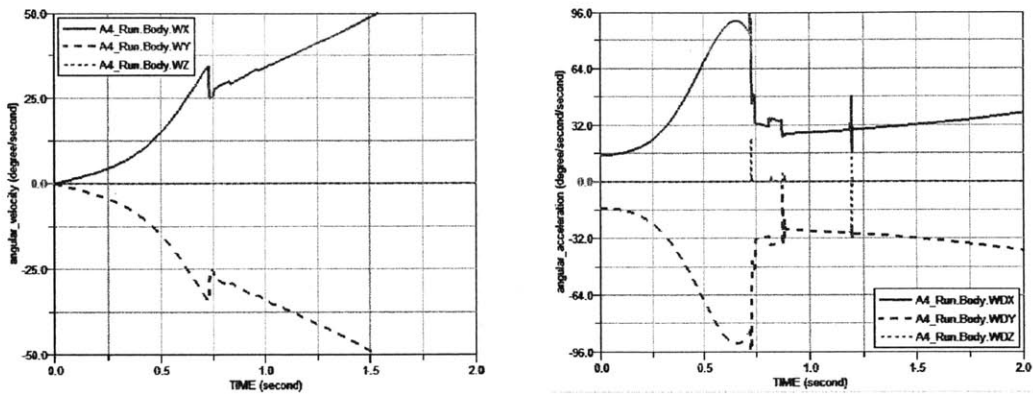


(a) Mid-deployment



(b) Final deployed state

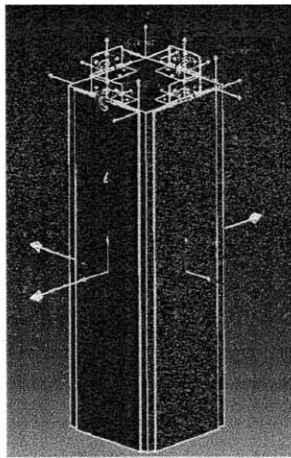
Figure 4-23: Short-edge deployable configuration with two panels stuck during deployment



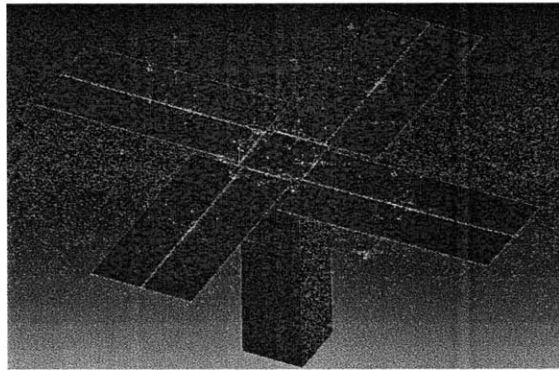
(a) Angular velocity about CubeSat CM (b) Angular acceleration about CubeSat CM

Figure 4-24: Dynamics of short-edge deployable with two panels stuck during deployment

4.3.4 Short-edge Deployable with Long-edge Coupled



(a) Stowed Configuration



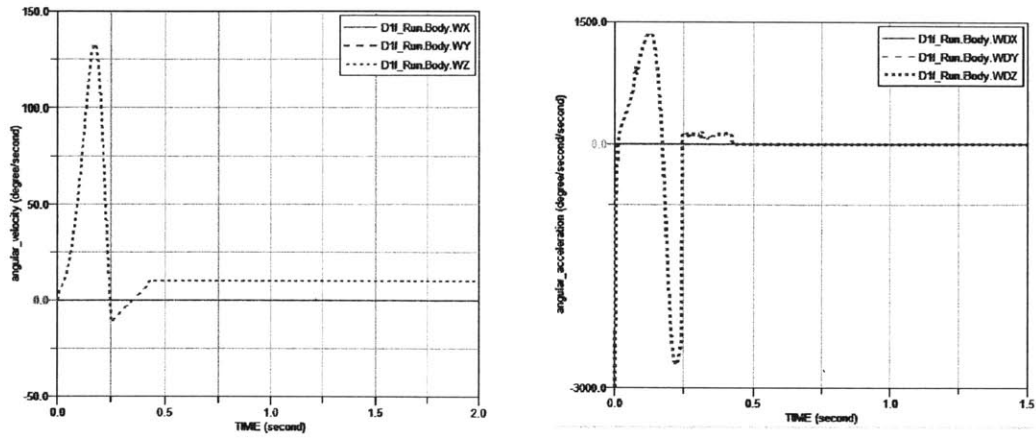
(b) Deployed configuration

Figure 4-25: Adams model of short-edge deployable panels with coupled long-edge panels

4.3.4.1 Normal Deployment

Figure 4-26 shows the angular velocities and accelerations resulting from nominal deployment of this configuration. At the end of deployment, the satellite has an

angular velocity of **10 deg/s** about the Z-axis. This is the only panel configuration that imparts any lasting motion on the satellite under normal conditions.



(a) Angular velocity about CubeSat CM (b) Angular acceleration about CubeSat CM

Figure 4-26: Dynamics of short-edge deployable with two panels stuck during deployment

Chapter 5

Conclusions

5.1 Summary of Key Results

The goal of this thesis was to investigate the forces, torques, and resulting motions associated with the deployment of various CubeSat solar panel assemblies. A numerical simulation was developed to model the deployment dynamics of a single solar panel, including impact with a locking feature in the hinge. The impact model showed acceptable accuracy when compared against a particular set of test data.

Deployment simulations of four commercial-off-the-shelf CubeSat solar panel assemblies were then developed using a professional multibody dynamics software package. Nominal and partial deployments were simulated and the trend lines were obtained for the evolution of the angular velocities and accelerations of the CubeSat for the duration of the deployment. The partial deployment simulations shed insight into the order of magnitude motions an attitude control system may need to mitigate in the event a solar panel fails to deploy.

5.2 Future Work

Due to time constraints, it was not possible to integrate panel flexibility into the multibody dynamics models. It would be extremely insightful if a future study were

to investigate the oscillations induced by both normal and asymmetric deployments of flexible 2U and 3U panels constrained along the short edge. These panels are of particular interest because of their low first-mode frequency. It is suspected that the impact force will excite the vibration mode of the panels, which could cause the entire CubeSat to oscillate about one or more axes. This could prove extremely problematic for imaging or optical communication missions that have tight pointing requirements and are susceptible to jitter.

Another interesting study would be to further investigate the resulting dynamics of off-nominal deployment cases of the fourth solar panel configuration discussed in this text. The complexity of that assembly makes it an extremely interesting subject for further rigid body dynamics studies.

Bibliography

- [1] Likins, P. W., "Finite element appendage equations for hybrid coordinate dynamic analysis," *International Journal of Solids and Structures*, Vol. 8, No. 5, 1972, pp. 709731.
- [2] Modi, V. J., "Attitude Dynamics of Satellites with Flexible Appendages- A Brief Review," *Journal of Spacecraft and Rockets*, Vol. 11, No. 11, Nov. 1974, pp. 743-751.
- [3] "CubeSat Design Specification Rev 13," Tech. rep., The CubeSat Program, Cal Poly SLO, San Luid Obispo, CA, Feb. 2014.
- [4] Blackwell, W., Allen, G., Galbraith, C., Leslie, R., Osaretin, I., Scarito, M., Shields, M., Thompson, E., Toher, D., Townzen, D., Vogel, A., Wezalis, R., Cahoy, K., Miller, D., Marinan, A., Kingsbury, R., Wise, E., Paek, S. W., Peters, E., Prinkey, M., Dav, P., Coffee, B., and Erickson, N., "MicroMAS: A First Step Towards a Nanosatellite Constellation for Global Storm Observation," *AIAA/USU Conference on Small Satellites*, Aug. 2013.
- [5] Smith, M., Seager, S., Pong, C., Knutson, M., Miller, D., Henderson, T., Lim, S., Brady, T., Matranga, M., and Murphy, S., "The ExoplanetSat Mission to Detect Transiting Exoplanets with a CubeSat Space Telescope," *AIAA/USU Conference on Small Satellites*, 2011.
- [6] Janson, S. and Welle, R., "The NASA Optical Communication and Sensor Demonstration Program," *AIAA/USU Conference on Small Satellites*, Aug. 2013.
- [7] Kuang, J., Meehan, P. A., Leung, A., and Tan, S., "Nonlinear dynamics of a satellite with deployable solar panel arrays," *International Journal of Non-Linear Mechanics*, Vol. 39, No. 7, Sept. 2004, pp. 1161-1179.
- [8] , E.-w. G., , X.-p. Z., and , Z.-q. Y., "Simulation and analysis of flexible solar panels deployment and locking processes," *Journal of Shanghai Jiaotong University (Science)*, Vol. 13, No. 3, June 2008, pp. 275-279.
- [9] Christensen, E. R. and Lee, S. W., "Nonlinear finite element modeling of the dynamics of unrestrained flexible structures," *Computers & structures*, Vol. 23, No. 6, 1986, pp. 819829.

- [10] Leissa, A. W., "Vibration of plates," Technical Report NASA-SP-160, NASA, Washington, DC, Jan. 1969.
- [11] Steinberg, D. S., *Vibration analysis for electronic equipment / Dave S. Steinberg*, New York : John Wiley & Sons, c2000., 2000.
- [12] Ferris, M. and Haslehurst, A., "The Use, Evolution and Lessons Learnt of Deployable Static Solar Array Mechanisms," *Proceedings of the 42nd Aerospace Mechanisms Symposium*, NASA Goddard Space Flight Center, Baltimore, MD, May 2014.
- [13] Marinan, A. D., *From CubeSats to constellations : systems design and performance analysis*, Thesis, Massachusetts Institute of Technology, 2013, Thesis: S.M., Massachusetts Institute of Technology, Department of Aeronautics and Astronautics, 2013.
- [14] Daniel Walter, K., "Techniques for using adams in spacecraft applications," ADAMS: Mechanical Dynamics-Customer Service, 16th European MDI User Conference, Berchtesgaden, Germany, 2001.
- [15] Budynas, R. G., *Shigley's Mechanical Engineering Design*, Science Engineering & Math, 9th ed., Jan. 2010.
- [16] Sneddon, I. N., "The relation between load and penetration in the axisymmetric Boussinesq problem for a punch of arbitrary profile," *International Journal of Engineering Science*, Vol. 3, No. 1, 1965, pp. 4757.
- [17] Chen., W., "The plastic indentation of metal block by a flat punch, September 1968 (70-12)," *Fritz Laboratory Reports*, Jan. 1968.
- [18] Fabrikant, V. I., "Flat punch of arbitrary shape on an elastic half-space," *International Journal of Engineering Science*, Vol. 24, No. 11, 1986, pp. 1731-1740.
- [19] Wise, E. D., Pong, C. M., Miller, D., Cahoy, K., and Nguyen, T. T., "A Dual-Spinning, Three-Axis-Stabilized CubeSat for Earth Observations," *AIAA Guidance, Navigation, and Control (GNC) Conference*, American Institute of Aeronautics and Astronautics, Aug. 2013.
- [20] Sinclair, D., "Picosatellite Reaction Wheels (RW-0.007-4)," 2013.
- [21] Sinclair, D., "Microsatellite Reaction Wheels (RW-0.06-7)," 2013.
- [22] "MAI-400 | Maryland Aerospace, Inc." .
- [23] "XACT: High Performance Attitude Control for CubeSats," .
- [24] "Micro Reaction Wheel: High Performance Attitude Determination for CubeSats," .
- [25] Sinclair, D., "Picosatellite Reaction Wheels (RW-0.01-4)," 2013.
- [26] Kalman, A., Reif, A., and Martin, J., "MISC 3: The Next Generation of 3U CubeSats," *AIAA/USU Conference on Small Satellites*, Aug. 2013.

- [27] "CubeSat deployable solar panel prototype test," Oct. 2011.
- [28] "Double Deployable Cubesat Solar Panel Environmental Test," Oct. 2011.
- [29] Bralower, H. L. H. L., *Mechanical design, calibration, and environmental protection of the REXIS DAM*, Thesis, Massachusetts Institute of Technology, 2013, Thesis: S.M., Massachusetts Institute of Technology, Department of Mechanical Engineering, 2013.
- [30] "General Environmental Verification Standard (GEVS) for GSFC Flight Programs and Projects," Technical Standard GSFC-STD-7000A, NASA Goddard Space Flight Center, Greenbelt, MD, April 2013.
- [31] Chatterjee, A., *Rigid Body Collisions: Some General Considerations, New Collision Laws, and Some Experimental Data*, Ph.d. thesis, Cornell University, Jan. 1997.
- [32] Slocum, A., *FUNdaMENTALS of Design*, Oxford University Press, Oxford, 2007.